RESEARCH ARTICLE

VOLCANICA

Decoding links between magmatic processes and eruption dynamics: whole-rock time series petrology of the 2021 Tajogaite eruption, La Palma

Jane H. Scarrow*[α], Matthew J. Pankhurst[β,γ,δ], Olivia A. Barbee[ε], Katy J. Chamberlain[ζ], Daniel J. Morgan[η], Marc-Antoine Longpré[θ,ι], Samantha Tramontano[κ], James Hickey[λ], David A. Neave[μ], Gavin K. Rollinson[λ], Alexander G. Stewart[μ], Penny E. Wieser[ν], Beverley C. Coldwell[β,γ], William Hernández[β], Luca D'Auria[β,γ], and Nemesio M. Pérez[β,γ]

[α] Department of Mineralogy and Petrology, University of Granada, Granada, Spain.
[β] Instituto Volcanológico de Canarias (INVOLCAN); San Cristóbal de La Laguna, Tenerife, Spain.
[γ] Instituto Tecnológico y de Energías Renovables (ITER), Granadilla de Abona, Tenerife, Spain.
[δ] Now at: Gaiaxiom, Copenhagen, Denmark.
[ε] Xnovo Technology, Køge, Denmark.
[ζ] School of Environmental Sciences, University of Liverpool, Liverpool, UK.
[η] School of Earth and Environment, University of Leeds, Leeds, UK.
[θ] Queens College, City University of New York, Queens, USA.
[ι] Graduate Center, City University of New York, New York, USA.
[κ] American Museum of Natural History, Theodore Roosevelt Park, New York, USA.
[λ] Department of Earth and Environmental Sciences, University of Exeter, Penryn, UK.
[μ] Department of Earth and Environmental Sciences, University of Manchester, Manchester, UK.
[ν] Department of Earth and Planetary Science, University of California, Berkeley, CA, USA.

Submitted: 2024-08-02 | Accepted: 2024-11-24 | Published: 2024-12-28

Abstract

We present an integrated petrological study of the 2021 Tajogaite eruption, La Palma, examining magmatic processes that initiated, sustained, and terminated surface volcanic activity. High temporal resolution sampling of near-continuously erupted alkali-basalt lava and tephra over the 85-day event reveals magma plumbing system dynamics from compositional trends. Initial deposits were mineralogically varied, reflecting mobilisation of shallow, evolved mush perturbed by fresh deep, primitive magma influx (Stage 1 - initiation). Transition to more primitive, uniform compositions recorded progressively deeper tapping of pre-existing magmatic zonation (Stage 2 - evacuation). The final stage (Stage 3 - waning) was characterised by more evolved magma compositions on the same fractionation trend as Stage 2, with tephra glass compositions suggesting a proportionately larger role of mush interstitial melts. We suggest this reflects shutdown of mantle-derived magma supply, a key process in eruption waning and termination, and compression-driven melt extraction of less mobile melts. Correlation with geophysical monitoring data demonstrates how near-real-time petrological monitoring could improve understanding of when an eruption may end.

Resumen

Presentamos un estudio petrológico integrado de la erupción de Tajogaite 2021, La Palma, que examina los procesos magmáticos que iniciaron, mantuvieron y pusieron fin a la actividad volcánica. El muestreo de alta resolución temporal de lava basáltica-alcalina y tefra, expulsadas casi continuamente durante 85 días, revela la dinámica del sistema magmático a través de tendencias composicionales. Los depósitos iniciales, mineralógicamente variados, reflejan la movilización de un sistema de magma rico en cristales, somero y evolucionado perturbado por la llegada de magma fresco primitivo profundo (Etapa 1 - iniciación). Una transición a composiciones más primitivas y uniformes registró un suministro gradualmente más profundo asociado a una zonación composicional preexistente en el sistema magmático (Etapa 2 - evacuación). En la etapa final (Etapa 3 - menguante), las composiciones magmáticas progresivamente más evolucionadas, con la misma tendencia de fraccionamiento que la Etapa 2, son más ricas en fundidos intersticiales que refleja el cierre del suministro magmático desde el manto y la extracción por compresión lo que representa un mecanismo para la disminución y término de la erupción. La estrecha correlación de los cambios magmáticos con las señales de monitoreo geofísicas demuestra cómo la monitorización petrológica podría mejorar la predicción del fin de una erupción.

Keywords: Lava, tephra, and glass time series; Petrological monitoring; Forecasting and hindcasting; Mush mobilisation; Filter pressing.

1 Introduction

When, and where, a volcanic eruption will start is typically the main focus of monitoring efforts. Another important question, however, is what may happen as an eruption progresses, and ultimately when it will end. Information about eruption cessation is fundamental as global volcanic risk is increasing [UNDRR 2022] and a substantial proportion of fatalities stemming from primary volcanic activity occur as a result of residents returning to known high-hazard zones during eruptive episodes [Barclay et al. 2019]. In this context, social drivers, such as place attachment, are exacerbated by uncertainties in forecasting and evolving eruptive style [e.g. Vergara-Pinto et al. 2024]. Whereas geophysical signals from complex mag-

* jscarrow@ugr.es

Editor: J. Browning | Typesetter: J. Farquharson

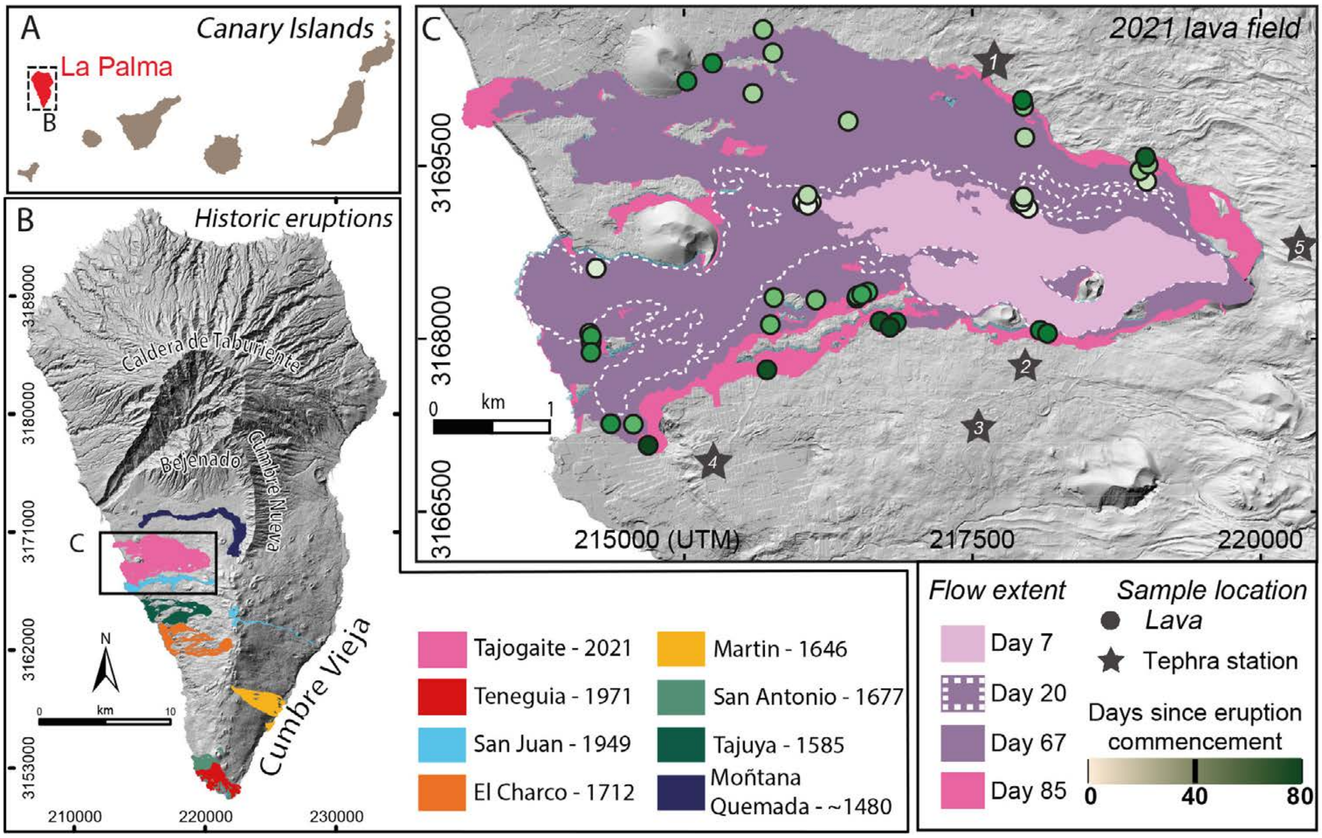

Figure 1: [A] Location of La Palma in the Canary Islands archipelago; [B] Historic eruptions on La Palma highlighting the cyclical nature of the volcanism [GVP 2022]. Tajogaite 2021 eruption: [C] Lava field extent, lava sample locations (circles) and tephra collection pit locations (numbered grey stars), most of the Longpré et al. [2024] tephra glass samples were collected from station 3. Many sample sites were inundated by later flows.

matic plumbing systems may become noisier once an eruption initiates, petrological 'signals' become available as compositions of volcanic rocks (magma), glasses (melt), and crystal cargoes record direct evidence of magma system dynamics which prime, drive, modulate, and halt eruptions [Blundy and Cashman 2008; Dosseto et al. 2010; Cassidy et al. 2018]. Specifically, connections between eruption dynamics, for example lava effusion and flow rates, and magmatic processes such as intrusion and rejuvenation, mush mobilisation, and filter pressing can be interpreted from well-characterised volcanic deposits [e.g. Cashman et al. 2017; Gansecki et al. 2019; Lissenberg et al. 2019; Bonadonna et al. 2022; Soldati et al. 2024]. In this way, petrology can access the past as well as the present, where other techniques cannot. Yet in the absence of detailed records, it can be challenging to place volcanic deposits into an unambiguous time sequence, and even more difficult to gauge eruption duration to consider when activity may end. Petrological monitoring of active eruptions, therefore, has obvious potential not only for understanding syn-eruptive processes with clear and immediate applications for risk assessment, hazard management and hence civil protection [e.g. Pankhurst et al. 2014; Gansecki et al. 2019; Re et al. 2021; Corsaro and Miraglia 2022; Pankhurst et al. 2022], but also to extract more reliable understanding from ancient deposits.

The long-standing goal of integrating petrological information with real-time data such as geophysical, gas geochemistry, and phenomenological monitoring has largely been conducted post-eruption [e.g. Kahl et al. 2013; Pankhurst et al. 2018], yet pioneering work by Devine et al. [1998] showed syn-eruptive petrological analysis provided critical insights to hazard assessment. The value of linking petrological studies with monitoring data to improve hazard assessment and forecasting was recently progressed by Kent et al. [2023]. They noted compositional information recorded in erupted products informs understanding of likely eruption initiation mechanisms, or 'triggers,' which are related to eruptive styles and timescales, information that is of direct relevance to future eruption risks. Petrological monitoring approaches can be divided into litho-sedimentological, petrographic and textural, and compositional [Re et al. 2021]. The first category includes grain size distribution, componentry analysis, clast shape, and morphology. The second group comprises petrographic studies using optical microscopy; crystallinity assessment, vesicularity analysis, crystal size distribution (CSD), and vesicle size distribution (VSD). The third group is composed of: major element composition of bulk rocks and groundmass glasses (e.g. X-ray fluorescence, XRF); trace element analyses (e.g. laser ablation inductively coupled plasma mass spectrometry, LA-ICP-MS); isotopic analyses (e.g. multicollector laser ablation

Figure 2: [A] Typical view of Strombolian lava fountaining during Stage 2; [B] Example of a tephra collection station set up; [C] Typical view of the lava flow field including an active channel and sampling of molten flow; [D] Quenching of lava sample in a metal bucket of cold fresh water; [E] Hand specimen of new lava, September 2021; [F] Lava under binocular microscope, field of view 3 cm; [G] Tephra fall deposit on a car bonnet, September 2021, field of view ~40 cm; [H] Ash under binocular microscope, field of view 3 cm. (photographs A–C by kind permission of Rafa Avero).

inductively coupled plasma mass spectrometry, MC-ICP-MS); melt and fluid inclusion major, trace elements (secondary ion mass spectrometry, SIMS), and volatile compositions (Fourier-transform infrared spectroscopy, FTIR); and diffusion chronology studies (electron microprobe analysis, EMPA).

During ascent to the surface, magma often undergoes lateral and vertical migrations spanning tens of kilometres before an eruption [Klügel et al. 2015; Sparks and Cashman 2017; Ebmeier et al. 2018]. Throughout this journey, varying degrees of magma mixing, mingling, crystal mush mobilisation, crystallisation, fractionation, and wall rock assimilation may occur. The whole-rock composition of volcanic products is an expression of the combined effects of these processes. Consequently, time series of whole-rock compositions provide a self-consistent signal of the salient physicochemical processes taking place within a sub-volcanic plumbing system during an ongoing eruption. Recent documentation and interpretation of time series petrological data from Hawaiʻi, Sicily, and Iceland have contributed to the monitoring of mafic eruptions. Links between the composition of volcanic deposits and magmatic processes were made for: lava from the 2018 Kīlauea eruption on Hawaiʻi [Gansecki et al. 2019]; volcanic glass compositions from the 2020–2021 eruption of Mount Etna, Sicily [Corsaro and Miraglia 2022; Corsaro et al. 2024]; and lavas, tephras, and melt inclusions from the 2021 Fagradalsfjall basaltic eruption, Iceland [Bindeman et al. 2022; Halldórsson et al. 2022]. At Kīlauea, changes in eruptive style were related to variations in lava compositions and temperature with initial fissure opening erupting more viscous, cooler, and more evolved basaltic lava that transitioned after a few days to less viscous, hotter, and more primitive lava [Gansecki et al. 2019]. By contrast, at Etna, initially more primitive compositions transitioned to explosive eruption of more evolved melts following magma mixing and fractional crystallisation [Corsaro and Miraglia 2022]. On Iceland, early heterogeneity to later homogeneity was linked to differences in vent activity, magma discharge rates, as well as pāhoehoe and ʻaʻā lava types [Bindeman et al. 2022], and deepening of magma tapping from relatively shallow depleted mantle reservoirs to more-enriched magma storage zones near the Moho was identified [Halldórsson et al. 2022]. As noted by Corsaro and Miraglia [2022], there is significant potential for erupted volcanic deposits to provide insights into the structure and pre-eruptive processes of the magmatic plumbing system and how these control volcanic behaviour during an eruption. For example, a textural and compositional study of the March 2015 Villarrica, Chile, lava fountain pyroclastic products by Romero et al. [2023] revealed a hot, deep, overpressured magma source before shallow overpressure led to lava fountaining; thus providing valuable insights into the architecture of volcanic plumbing systems and pre-eruptive physicochemical magmatic processes including mixing, crystallisation, assimilation, and degassing. Understanding such processes is critical for unraveling mechanisms behind volcanic eruptions and so predicting future volcanic behaviour. The key challenge is determining how information encoded in petrological datasets may be most efficiently exploited in future volcanic crises.

Here we present the most extensive compositional dataset of whole-rock major and trace elements and petrography for lava and tephra sampled on a near-daily basis throughout the 2021 Tajogaite eruption, La Palma, Canary Islands, Spain. Our petrological results are complemented with published tephra glass, representing quenched melt, sampled at the same or higher temporal frequency [Longpré et al. 2024]. Comparison is made with time-series trends and divisions identified in the same eruption on the basis of whole-rock compositional data [Day et al. 2022], lava groundmass [Ubide et al. 2023], and fluid inclusion microthermometry [Zanon et al. 2024]. Published Tajogaite mineral compositions are summarised [Castro and Feisel 2022; Day et al. 2022; Pankhurst et al. 2022; Romero et al. 2022; Dayton et al. 2023; Ubide et al. 2023; Bonechi et al. 2024], as are thermobarometric and geophysical indications of magma storage conditions and ascent rates [D'Auria et al. 2022; Fabbrizio et al. 2023; Bonechi et al. 2024; Zanon et al. 2024]. Combining these lines of evidence, we present a causative petrogenetic model that addresses development of the magma system feeding the eruption and how the sequence of magmas were tapped during the eruptive episode. The aim, at this time post-eruption, is to offer a comprehensive discussion that integrates our new data with the existing literature. To do this we summarise the petrological methods used to investigate the Tajogaite eruption, providing a guide for future monitoring efforts considering both traditional and innovative analytical techniques and highlighting the relevance of results from these. Importantly, a petrological signal heralding the end of the eruption is identified; this may have presented in other recent eruptions and could thus constitute a more widely applicable indicator of eruption behaviour.

2 Volcanological background

The Canary Islands are an intraplate volcanic archipelago located in the Atlantic Ocean, 100 km west of southern Morocco (Figure 1A). The seven main islands are, from east to west: Lanzarote, Fuerteventura, Gran Canaria, Tenerife, La Gomera, La Palma, and El Hierro. Magmatic activity, preserved as seamounts, commenced ~70 Ma on Jurassic ocean crust [Carracedo and Troll 2016] with the oldest subaerial activity decreasing in age east to west from 20 Ma on Lanzarote-Fuerteventura to 1.7 Ma on La Palma and 1.1 Ma on El Hierro [Carracedo and Troll 2016]. All islands have been active in the last 1 million years and four—Lanzarote, Tenerife, El Hierro, and La Palma—have had historical eruptions since the late 1400s.

La Palma comprises an extinct shield volcano in the north that includes the lowermost Garafía volcano (~1.7–1.2 Ma) overlain by the ~1.2–0.5 Ma Taburiente volcano. Overlapping with the final stages of Taburiente (~0.6–0.5 Ma: K-Ar and Ar/Ar [Carracedo et al. 2001; Guillou et al. 2001]) are both Bejenado volcano and Cumbre Nueva (K-Ar and Ar/Ar [Carracedo et al. 2001; Guillou et al. 2001]). The youngest expression of La Palma volcanism is the Cumbre Vieja Ridge in the south. The oldest confirmed eruptions along the Cumbre Vieja Ridge were at ~125 ka (K-Ar [Guillou et al. 1998]) with younger activity at 6050 BCE ± 1500 a (K-Ar [Guillou et al. 1998]; ^{14}C [Carracedo et al. 2001]), followed by a paroxysm at 4900 BCE ± 50 a (^{14}C [Carracedo et al. 2001]), and continuing intermittently through 4050 BCE ± 3000 a (K-Ar [Guillou et al. 1998; Day et al. 1999]); 1320 BCE ± 100 a (^{14}C and K-Ar [Guillou et al. 1998; Day et al. 1999]); and, 360 BCE ± 50 a (^{14}C [Carracedo et al. 2001]). Subsequent pre-historic eruptions include events at 900 CE ± 100 a (^{14}C [Day et al. 1999; Carracedo et al. 2001]) and 1481 CE ± 11 a (Guanche oral tradition [Hernandez-Pacheco and Valls 1982]), both with an estimated maximum volcano explosivity index (VEI) of 2 [Longpré and Felpeto 2021]).

Seven historical eruptions have been recorded on La Palma (Figure 1B). Observed events in 1585, 1646, 1677–1678, 1712, 1949, and 1971 all had a maximum VEI of 2 [Hernandez-Pacheco and Valls 1982; Longpré and Felpeto 2021]. Return periods vary between 22 and 237 years (Figure 1B), and eruption durations from 24 to 84 days. After 50 years of quiescence, the most recent eruption occurred in 2021 following just a week of accelerating unrest and lasted for 85 days, reaching a VEI of 3.

Typical of basaltic ocean islands with a relatively low magma supply, a shallow, <3 km (expressed throughout as below sea level), pervasive hydrothermal system identified from a spatially limited high Vp/Vs ratio (> 2) anomaly which could actually also result from rock fracturing [Di Paolo et al. 2020; D'Auria et al. 2022] is present at La Palma underlain by a vertically extensive and variably differentiated magma plumbing system, at ~30–7 km depth [Klügel et al. 2005; 2017; Amonte et al. 2022; D'Auria et al. 2022; Muñoz et al. 2022]. Changes in gas geochemistry and seismicity since 2017 can be considered as precursors to the 2021 eruption [Fernández et al. 2022; Padrón et al. 2022]. An increase in $^{3}He/^{4}He$, measured in cold mineral springs from 2017 onwards was interpreted as input

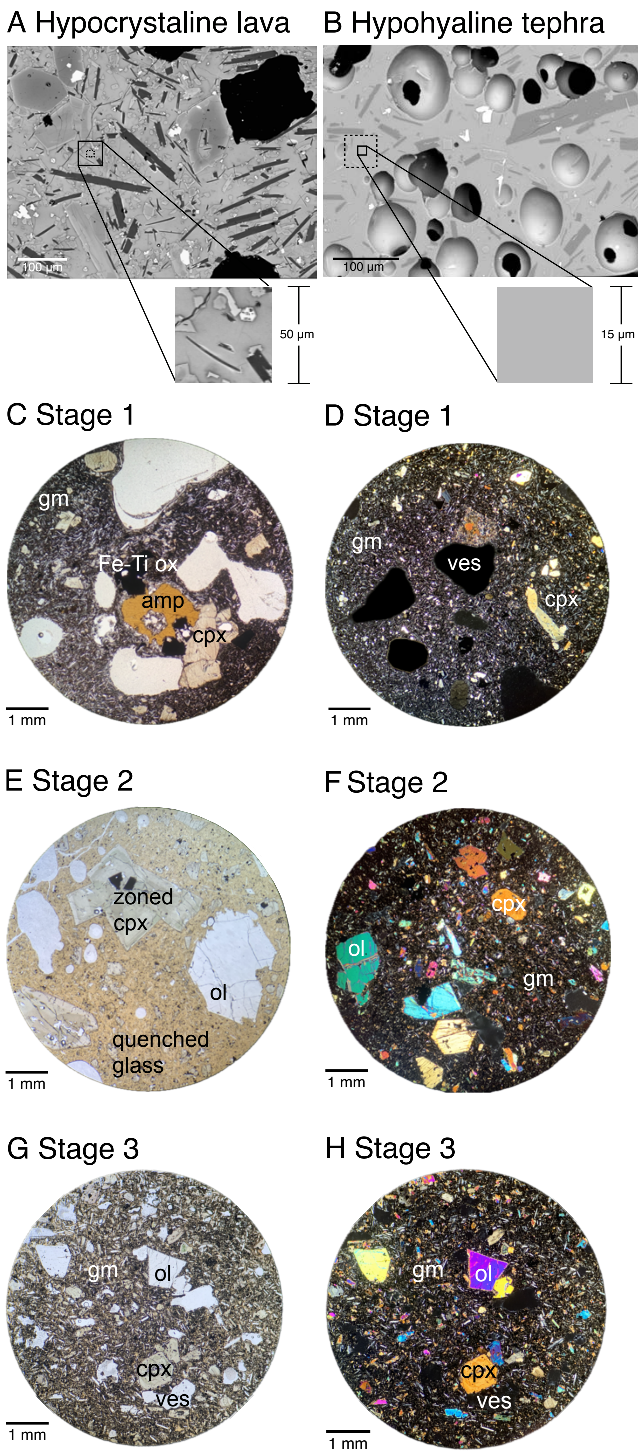

Figure 3: [A] Hypocrystalline lava texture (CAN_LLP_0084), electron back scatter image, note that Ubide et al. [2023] used a beam size diameter of 50 µm, marked by a black square and amplified in zoom, for the groundmass LA-Q-ICPMS analyses of major and trace elements, 15 µm dotted line square for comparison with B; [B] Glassy, hypohyaline tephra texture (CAN_LLP_0004), electron back scatter image, note that Longpré et al. [2024], used a 15 µm beam diameter, marked by a black square and amplified in zoom, for the electron microprobe major element glass analyses, 50 µm dotted line square for comparison with A; [C] Stage 1 lava (CAN_LLP_0001, ppl) showing macrocryst patchy compositional zoning, groundmass heterogeneity and partially resorbed amphibole disequilibrium texture, this sample was the first lava of the eruption to be sampled by the Canary Island Volcanological Institute (INVOLCAN); [D] Stage 1 lava (CAN_LLP_0001, xp) showing typical groundmass and clinopyroxene dominated Stage 1 mineralogy; [E] Stage 2 lava (CAN_LLP_0016, ppl) showing an increase in the modal proportion of olivine macrocrysts and a water-quenched groundmass texture, sample collection shown in Fig. 2C; [F] Stage 2 lava (CAN_LLP_0048, xp) note the increased abundance of olivine macrocrysts and more homogeneous groundmass texture compared with the Stage 1 lava in [C] and [D] [G] Stage 3 lava (CAN_LLP_0096, ppl) comparable abundance of olivine macrocrysts and homogeneous groundmass texture to Stage 2 lava in [E] and [F], this sample was the last lava of the eruption to be sampled by INVOLCAN; [H] Stage 3 lava (CAN_LLP_0096, xp). Abbreviations: cpx – clinopyroxene; ol – olivine; amp – amphibole, Fe-Ti-ox – Fe-Ti oxides; gm – groundmass; ves – vesicles; ppl plane polarised light; xp crossed polars.

of ^{3}He-rich less-degassed magma from depths of 30–25 km into magma pooled at 15–10 km [Padrón et al. 2022]. Seismic swarms also began in 2017 and continued through to June 2021; these were related to magma movement primarily detected at depths of 20–15 km, with some activity extending to 35 km [D'Auria et al. 2022; Fernández et al. 2022; del Fresno et al. 2023]. From September 11th–19th 2021, >300 earthquakes defined a previously unobserved shallow migration in seismicity shifting from ~13 to 8 km. During the same period vertical ground deformation above the hypocentres reached ~16 cm [Cabrera Pérez et al. 2022].

The Tajogaite eruption commenced on September 19th, ~2 km northwest of the 1949 Llano del Banco eruption site. Initial activity was explosive and marked by strong volcanic tremor. Lava erupted from a 200-metre-long fissure and a plume emitted SO_2-rich gas that reached 3 km height and tephra that reached heights of 1.5 km [GVP 2022]. Tephra cone building commenced around the main fissure vent and evolved into emission centres. The fissure-fed lava fountains formed lava flows that coursed to the west and west-southwest [Figure 2A–2B; Bonadonna et al. 2022]. These hybrid phenomena persisted with changing styles and intensity, maximum VEI 3, until the eruption ceased 85 days later.

As recorded in a Government Report [2022], the social and economic impacts of the Tajogaite eruption were locally extreme: >12 km^2 of urban and agricultural land were covered by 159 million m^3 of lava, 70+ km of roads were destroyed and ~3000 buildings severely affected by the lava and tephra. Over 7000 people were displaced. The damage to public and private assets exceeded 842 million euros. In addition to material and economic damage, other significant impacts include current and future effects on residents' physical—respiratory, ocular, dermatological—and mental health. Ecosystems, natural resources, and heritage have also been affected [Government Report 2022].

3 Sample collection and analytical methods

Lava was sampled on a near-daily basis, mostly from active fronts (Figure 1B) either as molten flows or solid incandescent blocks using a modified banana plantation support (~3 m steel pole welded with scrap metal to create a trident at one end and a flat hook at the other) and a metal bucket of water for quenching (Figure 2C–2D).

Careful inspection during reduction from multi-kilogram-sized samples at a local base, to smaller splits for petrographic and whole-rock analytical work off-island ensured representative samples were analysed. Continuous tephra air-fall collection sites were installed at strategic points around the volcano (Figure 1B and Figure 2B). Plastic containers, with 0.12–0.28 m^2 of collection surface area, were fixed to permanent structures with an unobstructed view of the sky. Most sites were accessed on a near-daily basis for sampling—the plastic container was unfixed and the collected tephra carefully swept into sample bags, and the container was then re-fixed. Petrological analysis of the lava and tephra included hand sample and thin section study, whole-rock major and trace element XRF, trace elements by ICP-MS, and quantitative evaluation of materials by scanning electron microscopy (QEMSCAN®).

Whole-rock compositions were analysed at the Scientific Instrumentation Centre, University of Granada, Spain. Major element determinations were measured by XRF, using a PANalytical Zetium, after fusion with lithium tetraborate. Typical one standard deviation precision, on analytical standards BE N, BHVO1, STM1, NimS, and JP1 was better than ± 1.5 % for an analyte concentration of 10 wt.%. Zirconium was determined by XRF on glass beads, with a precision better than ± 4 % for 100 ppm Zr. Trace elements were analysed by ICP-MS, using a NexION 300D, after HNO_3+HF digestion of 0.1000 g of sample powder in a Teflon-lined vessel at ~180 °C and 200 psi for 30 min, evaporation to dryness, and subsequent dissolution in 100 ml of 4 vol.% HNO_3. Instrument measurements were carried out in triplicate with a PE SCIEX ELAN- 5000 spectrometer using rhodium as an internal standard. One standard deviation precision, as determined from standards WSE, BR and AGV run as unknowns, was better than ± 2 % and ± 5 % for analyte concentrations of 50 and 5 ppm, respectively.

The QEMSCAN® analyses of thick sections were undertaken at Camborne School of Mines, University of Exeter, UK using a QEMSCAN® 4300 [Gottlieb et al. 2000]. Sample measurement and data processing was undertaken with `iMeasure v4.2SR1` and `iDiscover 4.2SR1` and `4.3` [Rollinson et al. 2011]. The QEMSCAN® operated at 25 kV, 5 nA, a 1000 X-ray count rate per pixel, a working distance of around 22 mm under high vacuum, and beam calibration every 30 minutes. Sample measurement used fieldscan measurement mode [Pirrie and Rollinson 2011] to analyse samples at an X-ray resolution/pixel spacing of either 5 or 10 µm and a 1000 μm^2 field size (×68 magnification).

QEMSCAN® data were processed to produce a phase map per sample, in which each distinct phase/composition was assigned an 8-bit pixel intensity value. 'Undifferentiated groundmass' was assigned to pixels that did not fit the strict raw data requirements needed to be assigned a mineral phase, and instead reflects a location of either glass or a combination of minerals below the pixel resolution. Isolated pixels of chemically complex phases such as amphibole may be regarded as the result of partial- or sub-volume interaction, i.e. between clinopyroxene, Ti-magnetite, plagioclase, and not a true representation of a mineral phase. Pixel intensities were used to create binary images for each phase/composition and conduct textural filtering and analysis in `Python` using the `numpy` and `skimage` libraries [van der Walt et al. 2014; Harris et al. 2020]. We chose an area of 10,000 μm^2 to reflect the minimum size of macrocrysts and assigned every connected region smaller than this limit to the groundmass. Phases that contributed ≥5 % macrocrysts by area in at least one sample were regarded as 'major', whereas the rest termed 'minor'.

Full data sets and analytical details are provided in Supplementary Material 1.

4 Results

Lavas are hypocrystalline and tephras partially glassy (hypohyaline, Figure 3A–3B). All samples have fairly primitive, >6 wt.% MgO, metaluminous, alkaline albeit modal feldspathoid-free, compositions (Figure 4A) with varied crystal cargoes and evidence of disequilibrium processes recorded in macrocrysts (Figure 3C). Macrocryst is used in preference to pheno/auto/ante/xenocryst, because it has no petrogenetic connotations but when referring to others' work we use their original terminology. The deposit has a mostly restricted compositional range. However, with the benefit of time-stamped samples and in particular early-erupted materials sampled before being inundated by later flows, we observe changes in whole-rock composition, mineral chemistry, and modal proportions through the eruption.

The results are presented as time series in chronological order and described with reference to three stages delineated by well-defined and co-varying compositional trends (Figure 5 and Figure 6): Stage 1 (0 to ~5 days since eruption start); Stage 2 (days ~7 to ~67), and Stage 3 (days ~70 to 85).

4.1 Petrography

Stage 1 is mineralogically complex with heterogeneous groundmass textures (Figure 3C–3D). The main mineral phase is clinopyroxene that exhibits variable concentric and sector zonation. Minor phases comprise olivine, plagioclase, variably resorbed amphibole and its reaction products (including rhönite and potassium feldspar), Fe-Ti oxides including prominent ilmenite, some biotite, as well as rare apatite and ultramafic and gabbroic micro-xenoliths (Figure 3C–3D). Stages 2 and 3 contain the same minerals as Stage 1 except they contain no amphibole nor any amphibole reaction products (Figure 3E–3H). An increase in olivine abundance and forsterite content and more homogeneous groundmass texture are also observed in Stages 2 and 3.

Quantitative mineral modal proportions for each of the three eruption stages are presented in Table 1, with a single sample from each stage considered representative of the relatively homogeneous mineral abundances and textures. In this study, macrocrysts were defined as those crystals with areas of ≥10,000 μm^2 hence with a minimum width of 100 µm

Table 1: Selected macrocryst phase abundances from samples representative of stages 1–3.

Stage	Sample	Area %			
		Clinopyroxene	Olivine	Amphibole	Plagioclase
1	CAN_LLP_0003D	8.5	0.4	0.6	3.4
2	CAN_LLP_0033E	11.7	5.1	0	0.2
3	CAN_LLP_0089D	12.5	4.4	0	0.8

(a natural break in grain size which permits close comparison with other work e.g. Ubide et al. [2023]). Macrocryst proportions change from Stage 1–2 and thereafter remain relatively stable.

4.2 Geochemistry

Figure 5 illustrates the whole-rock compositional ranges of the lava and tephra samples through the eruption, plotted together with tephra glass and groundmass data [Day et al. 2022; Ubide et al. 2023; Longpré et al. 2024, see also Supplementary Material 1] . The compositional variations in our three stages are summarised as:

- **Stage 1**: whole-rock lava compositions are relatively restricted with MgO ranging from 6.0 to 6.7 wt.% and SiO_2 from 44.2–44.6 wt.% (Figure 5A–5B).

- **Stage 2**: erupted lavas are progressively more primitive alkali basalts, starting with a rise in MgO (7.4 to 8.3 wt.%), and CaO, and decreases in Al_2O_3, Na_2O, K_2O, TiO_2, P_2O_5, and La/Yb. Notably, SiO_2 only increases slightly (44.2–45.1 wt.%; Figure 5A–5I and 5L). Stage 2 can be subdivided into substages A and B based on significant compositional inflections in the time series data occurring between days ~14 to ~19 that include plateauing in the increases in MgO, Cr, and Ni as well as the decreases in Al_2O_3, TiO_2, P_2O_5, Sr, and REE (Figure 5 and Figure 6A–6C). Second-order variations in the overall trend are detected within Stage 2 at day 30 when TiO_2 and P_2O_5 values stop decreasing and begin increasing, and at around day 56 when there is a minor increase in both MgO and Ni (Figure 5A, 5H, and 5I, and Figure 6B). By contrast, CaO and Sc concentrations and CaO/Al_2O_3 ratio increase steadily and continuously through Stage 2, whereas Na_2O, K_2O, Zr, Ba, Hf, Nb, and Th, in addition to Nb/Y and Th/Yb, decrease continuously (Figure 5J and Figure 6E–6K). On the other hand, SiO_2, FeOT, and K_2O/TiO_2 (Figure 5J) remain fairly constant throughout the whole of this stage, as does La/Yb through Stage 2B.

- **Stage 3**: a reversal of Stage 2 trends is observed to progressively more evolved alkali basalt lava compositions with MgO decreasing once more to ~8 wt.%. This stage initiated some two weeks before the eruption ended: concentrations of MgO, CaO, Ni, Cr, and Sc began to drop (Figures 5 and 6), whereas Al_2O_3, Na_2O, K_2O, Zr, Ba, Nb, La/Yb, and Nb/Y rose (Figures 5 and 6). As between the other stages SiO_2, FeOT, and K_2O/TiO_2 did not change significantly (Figures 5 and 6).

In Stage 1, compared to the lavas the tephra compositions tend to be slightly less primitive, with lower MgO (5.3–6.0 wt.%) and comparable or higher SiO_2 content (43.9–45.6 wt.%) (Figure 5). However, from Stage 2 onwards the tephra overlaps completely with the lavas for all major and trace elements. For this reason, lava and tephra are henceforth considered together as 'whole-rock compositions'. A ballistic bomb sampled during Stage 1 has the same composition as the lavas, whereas three ballistics collected during Stage 3 exhibit variable evolution (MgO 6.4-8.4 wt.%) compared to the lavas (MgO 8.0–8.7 wt.%) (Figure 5).

5 Results from other Tajogaite petrological studies

The time series trends observed in our compositional data are, on the whole, in agreement with data of Day et al. [2022] and Ubide et al. [2023] (Figures 5 and 6), with some minor and systematic differences: higher FeOT, Zr, Nb, Ni, and Nb/Y as well as lower Ba and La/Yb.

5.1 Complementary analytical approaches

Longpré et al. [2024] analysed glass within ash-sized tephra (Figure 3B) for major elements alone, by electron microprobe, at high temporal resolution through the eruption (Figures 5 and 6). Selected ash clasts were dominantly glassy, containing a mean of 26 ± 6 vol.% microcrysts (on a vesicle-free basis). Overall, glass composition was found to be independent of microcryst content, and therefore it provides a direct proxy for the composition of melt within the lava. The time-dependent glass compositions offer an opportunity in the present study to explore how coupled/de-coupled the carrier melt (minus the microlites that crystallised en route to/at the surface) was from the crystal cargo, and how that degree of coupling may have changed during the eruption. Compared to the lava and tephra whole-rock compositions the glass compositions follow the same general time series trends but are displaced to: higher SiO_2, Al_2O_3, Na_2O K_2O, and P2O5; lower CaO and MgO; and variable, initially lower then subsequently higher, FeO and TiO_2 (Figure 5). Variations in glass SiO_2 are more marked than in the whole-rock data. The increase in CaO in Stage 1 and subsequent decrease in Stage 3 are also more pronounced than in the whole-rock data. Marked increases in Na_2O and K_2O similarly indicate the onset of Stage 3.

Ubide et al. [2023] presented the composition of lava groundmass samples, analysed by raster-scanning areas of thin sections of lava and tephra using laser-ablation inductively coupled mass spectrometry (LA-Q-ICPMS). Notably, groundmass compositions measured by LA-Q-ICPMS were interpreted to represent erupted melts [Ubide et al. 2023]. To assess this conclusion ahead of discussion, we compare the

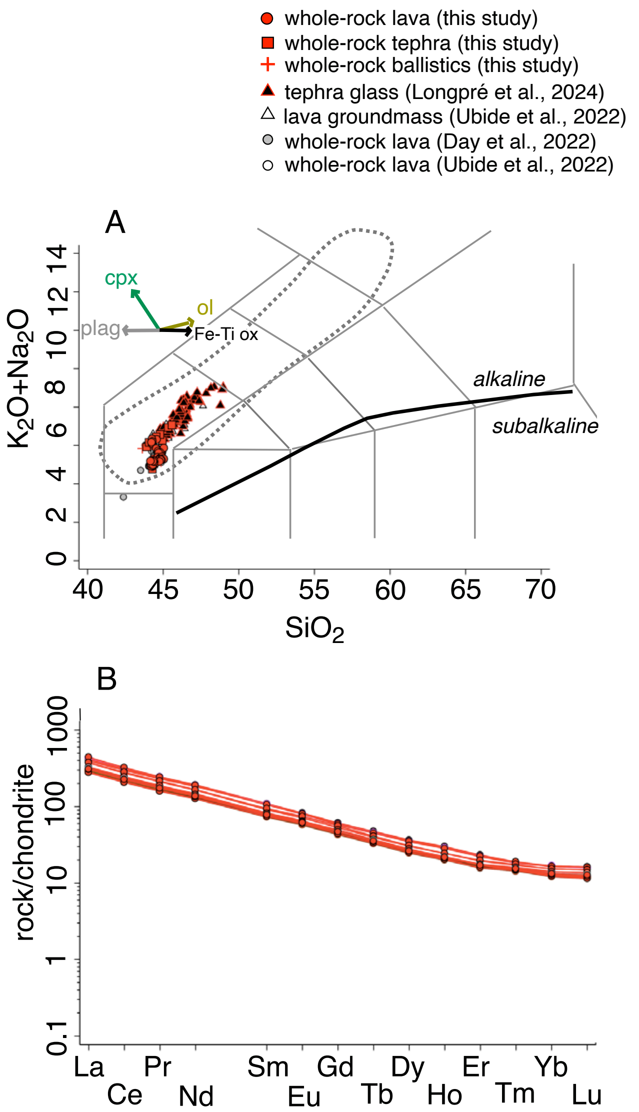

Figure 4: Tajogaite lava, tephra and glass whole-rock data. [A] Total Alkalis versus Silica (TAS). La Palma historic eruptions—field marked by a dashed line (data from Klügel et al. [2017]). Arrows indicate the direction in which fractionation of macrocryst minerals (data from Pankhurst et al. [2022]) will drive the whole-rock dataset, orientation determined from the least evolved, most Si-poor, lava compositions and displaced to the top left for clarity: cpx - clinopyroxene, ol - olivine, Fe-Ti ox - Fe-Ti oxides, plag – plagioclase. See Supplementary Material 1 for Harker diagrams of key major elements. All data are recalculated to 100 wt.% dry with Fe recalculated as FeOT, expressed as wt.%. [B] Chondrite-normalised whole-rock diagram (normalisation values of McDonough and Sun [1995]).

published groundmass compositions to the whole-rock and glass data (Figures 5 and 6). Relative to whole-rock lava and tephra, the groundmass has: higher SiO_2, Al_2O_3, Na_2O, K_2O, and P_2O_5 plus Zr, Hf, Y, Ba, Rb, Sr, Nb, U, Th and rare earth elements (REE); and lower CaO, FeOT, and MgO as well as Ni, Cr, Co, and Sc (Figures 5 and 6). By contrast, compared to the tephra glass compositions the groundmass has: comparable SiO_2, Al_2O_3, Na_2O, K_2O, and P_2O_5; but some key elements, CaO, MgO and in a few samples Al_2O_3, have higher values; whereas concentrations of FeOT, TiO_2, and MnO are lower. The larger spread of values for individual groundmass samples compared to the glass data (Ubide et al. [2023], their Figure 2, versus Figures 5 and 6 of this study) is an indication that variable proportions of different groundmass mineral phases were analysed, creating scatter.

Conspicuously, the largest discrepancies between glass and groundmass compositions are the higher concentrations in the latter of major elements that comprise a structural component of clinopyroxene, plagioclase, and Fe-Ti oxides (Figure 3). These variations are consistent with systematic over-sampling of microcrysts of these common mineral phases formed from magma that did not quench to glass, but rather to crystals, on emplacement (Figure 3A), and in this case do not capture the detail shown in the tephra glass data (Figure 3B, Longpré et al. [2024]). Therefore, groundmass compositions cannot simply be used as a proxy for glass/melt compositions and to do so could lead to errors in interpretation and calculations such as pressure and temperature of crystallisation from thermobarometers based on mineral-'melt' pairs. Furthermore, scatter in the groundmass data in all three eruption stages conceals compositional inflections detected in the whole-rock (magma) and glass (melt) compositional time series (Figures 5 and 6). For this reason, it would not be possible to detect the eruption stage transitions from the groundmass analyses alone, in the absence of lava whole-rock and tephra glass data.

5.2 Time-series trends and divisions

Three studies have been published [Day et al. 2022; Ubide et al. 2023; Zanon et al. 2024] which consider petrological time-series datasets that allowed those authors to differentiate different periods during the Tajogaite eruption (Figures 5 and 6). However, because their divisions are defined using varying criteria and rationale, the number of, and date ranges for, the stages differ. To support later discussion and interpretation, we first summarise their results and conclusions here as follows.

Based on whole-rock lava major and trace elements and $^{187}Os/^{188}Os$ measurements, Day et al. [2022] defined two stages. Their Stage 1 (day 0–20) was initially characterised by relatively low MgO (~6 wt.%) and elevated TiO_2 (~4 wt.%) concentrations in lavas which contained amphibole crystals and gabbroic micro-xenoliths, and then transitioned to more mafic, amphibole-free, compositions. The $^{187}Os/^{188}Os$ ratios were variable during the first stage. Stage 2 (day 21–85) was defined by a change to more MgO-rich whole-rock compositions and a progression to less radiogenic whole-rock $^{187}Os/^{188}Os$ interpreted to result from sourcing of deeper, more primitive, magma [Day et al. 2022]. The change in $^{187}Os/^{188}Os$ occurred during the first 20 days of the eruption then stabilised through Stage 2 with bimodality, attributed to crustal or anthropogenic contamination, evidenced by one sample erupted on day 42 (and another on day 77) followed by gradual exhaustion, through to the end of the eruption, of stored magma fractionated prior to the paroxysm.

By contrast, analyses of lava groundmass major and trace element and radiogenic isotope compositions by Ubide et al.

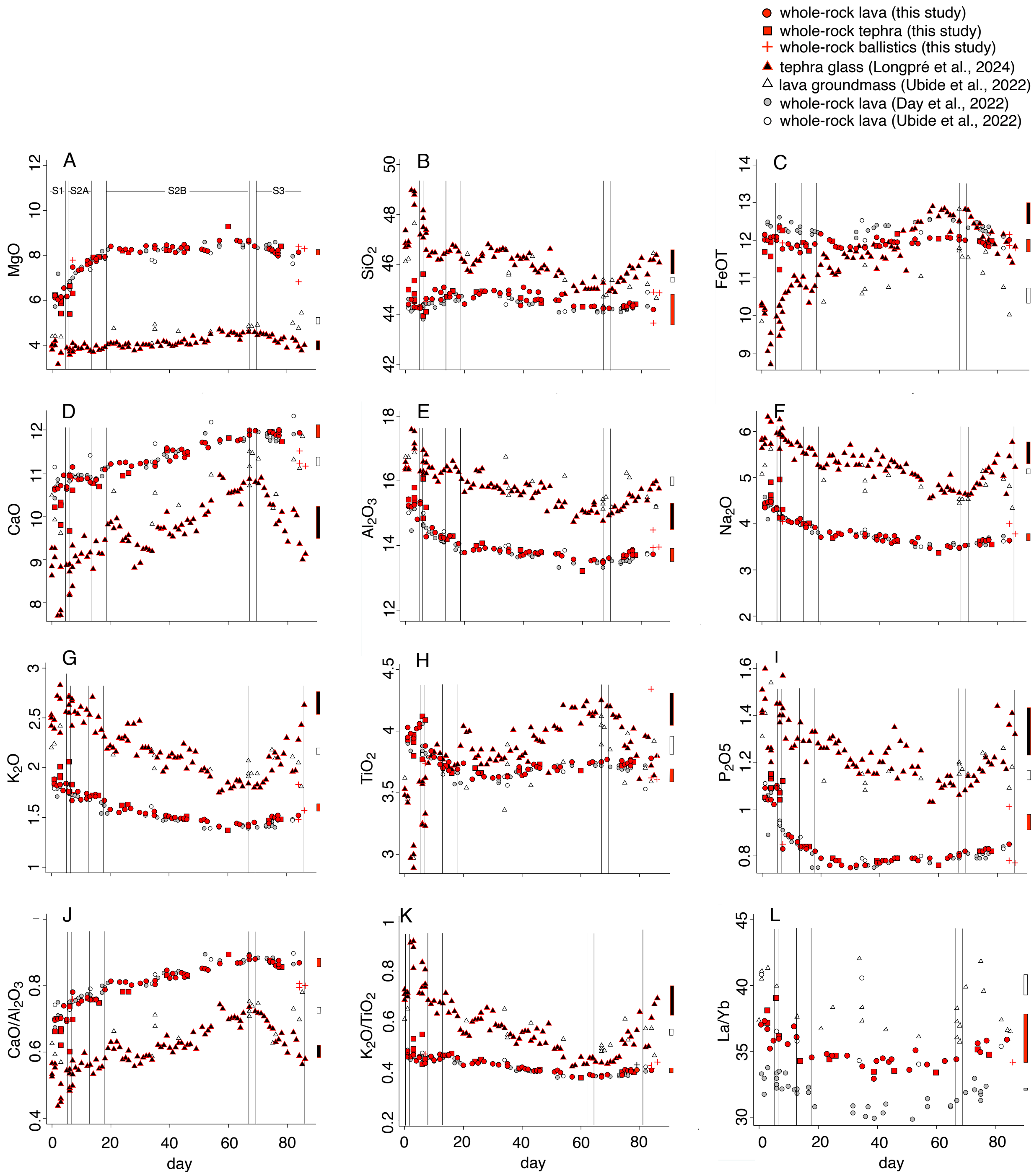

Figure 5: High-frequency time series major element compositions and trace element ratio for whole-rock lava and tephra plus tephra glass and groundmass. [A] MgO, Vertical fine lines mark stage boundaries: S1 - Stage 1; S2A - Stage 2A; S2B - Stage 2B; S3 - Stage 3; [B] SiO2; [C] FeOT; [D] CaO; [E] Al2O3; [F] Na_2O; [G] K_2O; [H] TiO_2; [I] P_2O_5; [J] CaO/Al_2O_3; [K] K_2O/TiO_2 [L] La/Yb. Major element oxides are expressed in wt.% and trace elements in ppm. Error bars shown as vertical lines on the right hand side of each graph: red - whole-rock data from this study, 2 standard deviations (sd) on repeated measurements of international standards BE N, BHVO1, STM1, NimS, and JP1 was better than ± 3.0 % (2 sd) for an analyte concentration of 10 wt.%, zirconium was determined by XRF on glass beads, with a precision better than ± 8 % (2 sd) for 100 ppm Zr (major element error values for Day et al. [2022] have comparable errors ± 4 % (2 sd) to XRF data measured in this study); grey - Day et al. [2022] data, uncertainties on ICP-MS measurements, in L, are less than ± 10 % (2 sd, their supplementary data Table 1); black - Longpré et al. [2024] glass data, 2 standard deviations calculated for means of repeated measurements of each glass spot for comparability with Ubide et al. [2023]; white - Ubide et al. [2023] groundmass data, 2 standard error values calculated for each volcanic matrix raster (data supplied by Ubide, personal communication). With the benefit of the full time series, reservoir collapse became evident in major element trends ~two weeks prior to the end of the eruption (Figures 5 and 6).

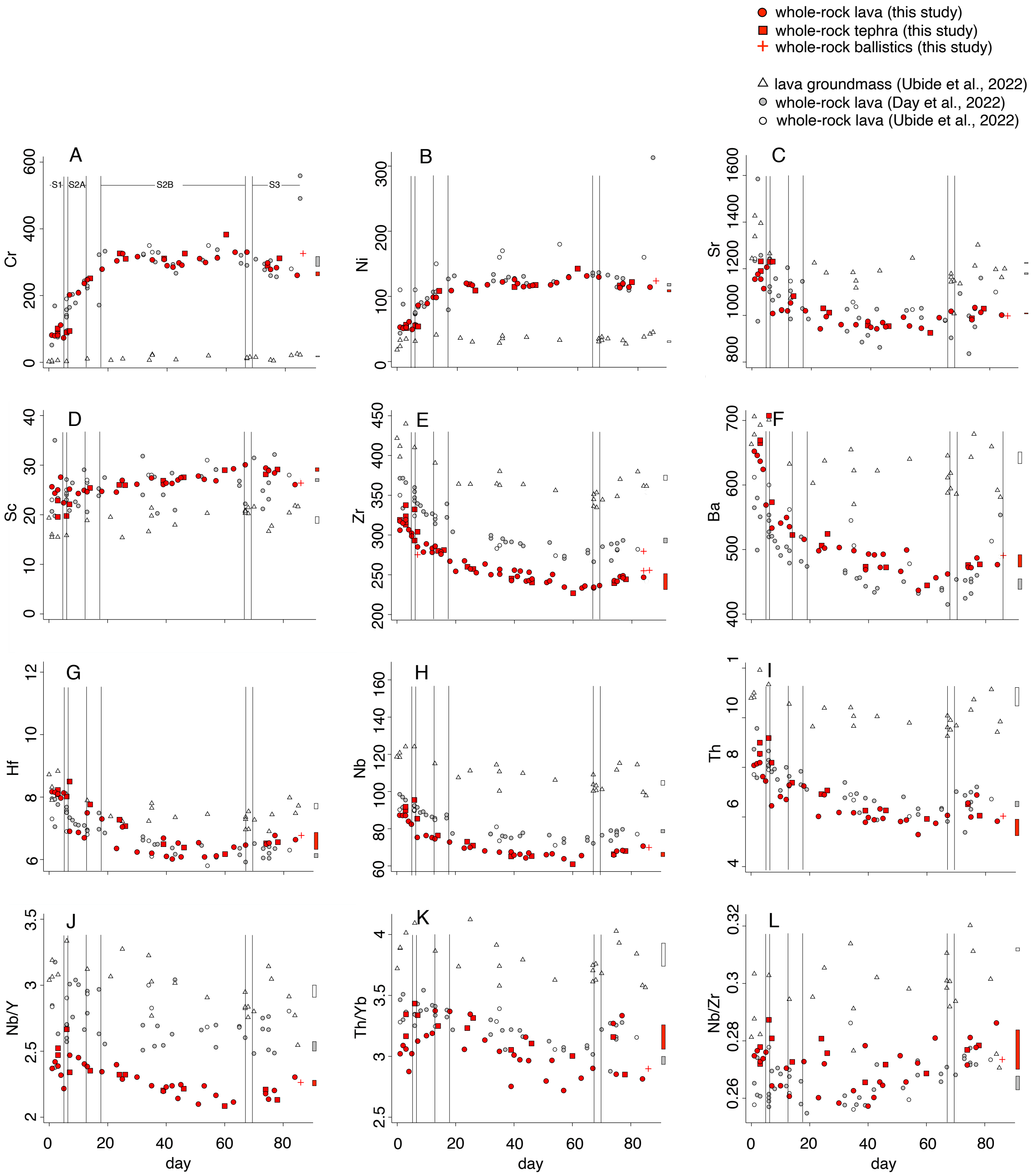

Figure 6: High-frequency time series trace element compositions for whole-rock lava and tephra plus tephra glass and groundmass. [A] Cr; [B] Ni; [C] Sr; [D] Sc; [E] Zr; [F] Ba; [G] Hf; [H] Nb; [I] Th; [J] Nb/Y; [K] Th/Yb; [L] Nb/Zr. Trace elements are expressed in ppm. Errors as in Figure 5: red - whole-rock data from this study, 2 standard deviations (sd) as determined from standards WSE, BR and AGV run as unknowns, was better than ±2 % and ±5 % for analyte concentrations of 50 and 5 ppm, respectively; grey - Day et al. [2022], black - Longpré et al. [2024] and white - Ubide et al. [2023] as in Figure 5. Vertical fine lines mark stage boundaries: S1 - Stage 1; S2A - Stage 2A; S2B - Stage 2B; S3 - Stage 3.

[2023] led them to identify four eruptive stages. They concluded the initial Phase 1 activity (days 0–8) remobilised an amphibole-bearing mush. Following this, through Phase 2 (days 9–43) the magma became more mafic and less radiogenic, with lower $^{87}Sr/^{86}Sr$. Then Phase 3 (days 44–67) was marked by a split in magma $^{87}Sr/^{86}Sr$ compositions to highly radiogenic and less radiogenic, although the values mostly overlap [Ubide et al. 2023, see extent of lines in box and whisker plots of their Figure 2], considered to represent discrete pulses of magma ascending through separated conduits. Their Phase 4 (days 68–85) commenced with a compositional change to more evolved compositions. This shift was interpreted to reflect switching from deep magma supply to fractional crystallisation which was invoked as the process driving the termination of the eruption.

Zanon et al. [2024] also separated the eruption into four phases on the basis of fluid inclusion microthermometry on olivines, clinopyroxenes and amphiboles. Phase 1 (days 0–8) was interpreted as emptying of an intermediate, 16.5–13 km depth, magma accumulation zone. They suggested the reactivated magmatic system was either a remnant of the 1949 eruption or early pre-2021 eruptive intrusion recorded in the seismicity that initiated in 2017. During their Phase 2 (days 9–35), they proposed that hotter, more olivine rich magma pulses, which they calculated were sourced from 27–22 km, ascended and partially re-equilibrated in the intermediate accumulation zone. Phase 3 (days 36–61) was interpreted to record eruption of a new pulse of magma based on a division of olivine fluid inclusion compositions: apparently high pressure, CO_2+H_2O+CO+N_2-bearing inclusions; and, contemporaneously, CO-N_2-free inclusions. The second type of fluid inclusions were interpreted to record the same magma that erupted during Phase 2. The occurrence of two fluid inclusion compositions in the system was linked to the bimodality of groundmass Sr isotope values [Ubide et al. 2023] and variation in whole-rock Os isotopes [Day et al. 2022], despite these compositional changes not coinciding in timing and the Sr and Os variations not being related to a variation in magma source depth. During Phase 4 (days 62–85), olivine with both deep, N_2-bearing, and shallow, N_2-free, fluid inclusions continued to erupt. Through to late November magma was interpreted to ascend from ~30 km with active intermediate level ponding only evident until the end of the month.

6 Results from other Tajogaite mineralogical studies

6.1 Mineral chemistry

Pankhurst et al. [2022] presented a summary of the mineralogy and mineral chemistry of the early erupted lavas. The most abundant macrocryst phase is titanaugite clinopyroxene, with concentric and sector zoning; olivine ($Fo_{78–80}$) is present as euhedral-anhedral isolated crystals; Fe-Ti oxides comprise both Ti-magnetite (3–5 wt.% TiO_2) and ilmenite; kaersutitic amphibole has distinct reaction rims indicative of disequilibrium; and groundmass is composed of fine-grained equivalents of the macrocryst phases plus plagioclase ($An_{58–67}$).

In the early to the middle-later lavas olivine became more Mg-rich (Fo_{79}–Fo_{81} to Fo_{80}–Fo_{86}) and Ni-rich (909–1246 ppm to 1228–2207 ppm) [Day et al. 2022; Dayton et al. 2023]. Many clinopyroxene grains have sieve textures with patchy and concentrically normal and reverse zoning [Zanon et al. 2024]. The reverse zoned clinopyroxene grains have sodic ferroaugite cores surrounded by 100+ µm titanaugite rims [Ubide et al. 2023] that are richer in SiO_2 and MgO, and poorer in TiO_2, Al_2O_3, and Na_2O [Pankhurst et al. 2022; Romero et al. 2022]. The zoning clearly reflects temporal changes in magma composition and temperature, although, it is not yet clear when the rims formed because such compositional variations may persist for extended periods under magmatic conditions [e.g. Nakagawa et al. 2002; Xing and Wang 2020]. Day et al. [2022] concluded the major and trace element abundances in clinopyroxene were variable (also see the following section, below) but that they did not show systematic changes between the early, middle, and late lavas. Nonetheless, Ubide et al. [2023] detected an increase in Cr_2O_3 in the clinopyroxene rims and microcrysts over time, although, once more, mean compositions are presented and ranges overlap [Ubide et al. 2023, their Figure 2]. Consistent with the trend in the ferromagnesian minerals, there was also a temporal change to higher anorthite content in the plagioclase microcrysts over time to labradorite-bytownite, although, significantly, the anorthite content drops once more towards the end of the eruption [Ubide et al. 2023].

6.2 Magma storage conditions, thermobarometry, and calculations

Based on changes in seismicity, ground deformation, and gas geochemistry Day et al. [2022] proposed magma was emplaced in the upper lithosphere, 8–45 km, some four to ten years before the 2021 volcanic activity commenced. During the eruption D'Auria et al. [2022] constrained the crustal structure and magma sources geometries from 3D distributions of P- and S-wave velocities identifying: a region of shallow, <3 km, hydrothermal alteration/fracturing; ocean crust to ~10 km depth; and, from 25 to 7 km, an extensive sub-crustal magma intrusion zone from which the Tajogaite eruption was fed. Various lines of thermobarometric evidence from Tajogaite lava and tephra crystal cargoes broadly align with shallow and deep seismic clusters constrained by the geophysical data. Comparable conditions of magma storage and crystallisation are given by various mineral and melt calculation methods.

The results and direct conclusions from published thermobarometric studies using mineral, melt, and fluid inclusion composition methodologies are described here ahead of their discussion. Castro and Feisel [2022] used tephra clinopyroxene microphenocryst rims plus microlite—matrix glass compositions to calculate temperatures of 1160–1170 °C and pressures of 7–10 kbar using equation 33 of Putirka [2008] and the barometer of Neave and Putirka [2017] assuming H_2O = 0 wt.%. They converted these pressures to to depths of 24–34 km using Putirka [2008] values of 2900 $kg\,m^{-3}$ and 3300 $kg\,m^{-3}$ densities for crust and mantle, respectively. Clinopyroxene core calculations yielded hotter temperatures, ~1200 °C, and pressures of ~9 kbar, ~31 km. Under hydrous conditions of ~0.8 wt.% H_2O both clinopyroxene and plagioclase microcryst-glass compositions temperatures were ~10 °C lower but pressures changed by only 0.1 kbar. Similarly, hydrous 1.5–2.7 wt.% H_2O clinopyroxene-melt thermobarometric calculations by Romero et al. [2022] using the same thermobarometer equations gave temperatures of ~1125–1158 °C and pressures of 6.7–11.7 kbar (26–40 km, converted using crust and mantle densities of 2800 and 3111 $kg\,m^{-3}$, respectively [Ranero et al. 1995; Tenzer et al. 2013]). By contrast plagioclase-melt analyses by these same authors gave lower temperatures, ~1090–1116 ± 36 °C, but higher pressures of 10.8–15.2 ± 2.8 kbar (36.9–51.4 ± 10 km) for both phenocrysts and microphenocrysts rims and cores, although plagioclase thermobarometry has recently been shown to be unreliable [Wieser et al. 2025]. Further clinopyroxene-liquid thermobarometry by Ubide et al. [2023] paired phenocryst rims and microcrysts with equilibrium groundmass, as a melt proxy, to calculate relatively constant thermobarometric conditions through the eruption. Use of groundmass compositions to represent melt may well be the cause of the discrepancy between the Ubide et al. [2023] and other values because the groundmass is neither a textural (Figure 3A and 3B) nor compositional (Figure 5) proxy for melt. These authors use the thermobarometers of Putirka et al. [2003] which are insensitive to H_2O, giving a pressure of 5.3 ± 1.5 kbar (20 ± 5.7 km) and temperature of 1125 ± 16 °C (they converted pressures to depths using a single local crustal density of 2697 $kg\,m^{-3}$, resulting in 10 % greater depth than the aforementioned conversion values). Ubide et al. [2023] also tested iterative calculations of the Putirka et al. [2003] barometer with the H_2O-sensitive thermometer of Putirka [2008, Equation 33]. Calculated temperatures decreased with an increase in water contents from 1–3 wt.% H_2O: 1129–1097 ± 18 °C and pressure varied 5.4–4.5 ± 1.5 kbar (20.4–17 ± 5.7 km). In agreement with previous results, Bonechi et al. [2024] calculated clinopyroxene phenocryst and microphenocryst crystallisation temperatures and depths, using a range of thermobarometers, as ~1100–1160 °C (1–3 wt.% H_2O) and ~10–30 km (crustal and mantle densities from Ranero et al. [1995] and Tenzer et al. [2013], respectively).

Olivine-hosted CO_2-rich fluid inclusion densities measured by Raman spectroscopy record depths of 15 to 24 km at the start of the eruption deepening to 27 km as the eruption progressed [Dayton et al. 2023, using the same Ranero et al. [1995] and Tenzer et al. [2013] crustal and mantle densities as above]. Dayton et al. [2024] expanded this work analysing volatile concentrations (H_2O, CO_2, fluorine, chlorine, sulfur) in melt inclusions to determine pre-eruptive pressures of 4.5–8.5 kbar, ~15–30 km, and major and trace elements in olivine-hosted melt inclusions that record fractional crystallisation and magma replenishment. By contrast, Burton et al. [2023] calculated the H_2O and CO_2 volatile contents of melt inclusions in olivine correspond to shallower, near Moho, entrapment pressures of at least ~2.90 to ~3.50 kbar (10.6–13 km depth, pressure to depth conversion using the local crustal density structure, crustal density: 2800 $kg\,m^{-3}$ and mantle density: 3200 $kg\,m^{-3}$, from D'Auria et al. [2022]). However, their calculated saturation pressures did not account for CO_2 present in the vapour bubble of melt inclusions, which explains the lower pressures than Dayton et al. [2024] who found >36–70 % of the total CO_2 was sequestered within the bubbles.

Variations in magmatic volatiles were also tracked through the eruption by He-Ar-CO_2-N_2 elemental and He-Ar-Ne isotopic compositions of fluid inclusions hosted in olivine and pyroxene phenocrysts of the erupted lava [Sandoval-Velasquez et al. 2023]. Results attest to magma storage at 6–12 km and 15–30 km (pressure conversion using a crustal density of 2800 $kg\,m^{-3}$ and mantle density of 3300 $kg\,m^{-3}$, from Zanon et al. [2024]). Analogously, olivine-, clinopyroxene-, and amphibole-hosted fluid inclusion microthermometric measurements of N_2 and CO mantle outgassing tracers revealed deepening of the magma source from 27 to 31 km (pressure to depth calculations densities used: shallow lavas 2350 $kg\,m^{-3}$, dense gabbroic xenoliths 3655 $kg\,m^{-3}$; mantle lithologies: 3115 to 3390 $kg\,m^{-3}$ [Klügel et al. 2005; Galipp et al. 2006]) over the course of the eruption [Zanon et al. 2024], with some evidence of sourcing down to 40 km and magma ponding in two regions; at 22–27 km and 4–16 km.

Phase equilibrium experiments and thermodynamic calculations were also used to constrain pre-eruptive conditions [Fabbrizio et al. 2023]. Comparison of results from these two approaches calculated the crystallisation temperature of olivine, clinopyroxene and oxide as ~1100 °C (3 wt.% H_2O) at 8–12 km (pressure to depth conversion densities from D'Auria et al. [2022]) – comparable to shallow estimates from other methodology.

In summary, pooled pre-eruptive magma flushed out by the deep magma supply, and its fluids ahead of its ascent [Cabrera Pérez et al. 2022], included olivine-poor alkali basalt crystallised at 6–16 km depth erupted during Stage 1 [Romero et al. 2022; Fabbrizio et al. 2023; Bonechi et al. 2024]. Stage 2 transitioned to a more olivine-rich, primitive, alkali basalt derived predominantly from ~25 km with some evidence of sourcing down to 40 km [Castro and Feisel 2022; Day et al. 2022; Romero et al. 2022; Fabbrizio et al. 2023; Ubide et al. 2023; Bonechi et al. 2024]. A difference in crystallisation depth has not been detected in Stage 3. Seismic clustering at ~10–16 km and ~22–27 km [D'Auria et al. 2022] and CO_2-rich fluid inclusions [Burton et al. 2023; Dayton et al. 2023; Sandoval-Velasquez et al. 2023; Zanon et al. 2024] correspond to the mineral crystallisation depths.

The 2021 eruption magma storage depths are consistent with the most recent historic eruptions on La Palma. Applying clinopyroxene-melt barometry Klügel et al. [2000] concluded the 1949 magmas were stored in the upper mantle, fractionating clinopyroxene, olivine, kaersutite, and Ti-magnetite at 24–33 km (8–11 kbar) and 18–24 km (6–8 kbar); then, following ascent into the rift system shallower storage and evolution occurred at 6–10.5 km (2–3.5 kbar). The 1971 Teneguía eruption magma was apparently initially stored relatively deep in the oceanic lithospheric mantle, 20–45 km (clinopyroxene-melt [Barker et al. 2015]). Barker et al. [2015] attributed the progressive deepening of the magmatic system since the 1949 eruption to underplating beneath the Cumbre Vieja rift zone. As the plumbing system developed, magmas were stored at a shallower depth, between 20 and 35 km. However, Barker et al. [2015] used whole-rock compositions as liquid compositions in thermobarometric calculations which most likely resulted in greater pressures than Klügel et al. [2000]. So, the deepening since 1949 is highly speculative.

6.3 Magma ascent rates

Travel-time seismic tomography based on >11,000 earthquake measurements led D'Auria et al. [2022] to conclude the Tajogaite magma rose rapidly, in <7 days, from the base of the oceanic crust at ~10–12 km to the surface [Przeor et al. 2024]. Accordingly, combining seismicity and macrocryst fluid inclusion data Zanon et al. [2024] estimated ascent rates of 0.01–0.1 $m\,s^{-1}$. These rates vary from slower movement, 0.01–0.04 $m\,s^{-1}$ (approximately 0.04–0.15 $km\,hr^{-1}$ or 1–3.6 $km\,day^{-1}$), between the deep (27–22 km) and intermediate (~16 km) magma zones, to faster rates of 0.05–0.1 $m\,s^{-1}$ (approximately 0.18–0.36 $km\,hr^{-1}$ or 4.4–8.6 $km\,day^{-1}$) from shallow (7–4 km) ponding zones.

By contrast, Bonechi et al. [2024] calculated ascent rates from crystal size distribution (CSD)–based mineral growth estimates of plagioclase microphenocryst size distribution, which at ~0.01–0.3 $m\,s^{-1}$ were three times faster than those quantified from either geophysical or fluid inclusion constraints. The faster rates are in agreement with those calculated from microlite number density [Romero et al. 2022], predicting groundmass plagioclase residence times of minutes. Accordingly, Fabbrizio et al. [2023] calculated that plagioclase microcrysts crystallised both en route to the surface, <1 km, and at the surface. In addition, from modelling of C-H-O-S solubility during decompression and a high concentration of deep-sourced CO_2 in the central vent, Burton et al. [2023] concluded exsolved gas ascended rapidly compared with shallower exsolved H_2O and SO_2 degassing from side vents.

In agreement with Tajogaite ascent rates, study of diffusion kinetics in olivine phenocrysts led Klügel et al. [2000] to conclude the 1949 basanite and erupted tephrite ascended from mantle depths within hours to days without protracted storage in crustal reservoirs. By contrast, compositionally varied clinopyroxene phenocrysts in the 1971 lavas indicated frequent pooling during ascent with magma pockets amalgamated shortly before eruption [Barker et al. 2015].

7 Discussion

Applying insights from volcanic deposits as a basis for real-time forecasting of the evolution of an eruption has been hampered by a lack of sufficiently complete multi-disciplinary data streams from the same eruption. Nevertheless, detailed lava and tephra compositional time series, such as those described above, may lead to breakthroughs in understanding of volcanic processes and signals offering valuable insights that are translatable to other monitoring approaches. The urgent need for such applications is underlined by, amongst other recent notable eruptions: renewed activity in southwest Iceland, Fagradalsfjall (March–September 2021, August 2022 and July–August 2023), and Svartsengi (December 2023–continuing); and recent activity in Hawai'i, Kīlauea, including the first eruption of Mauna Loa since 1984 (November 2022) and a new eruption within the Halema'uma'u crater (December 2020–May 2021 and September 2021–September 2023), with reinitiation of activity again in June 2024. Compounding these concerns related to future volcanic crises, is the recent identification of a low seismic wave velocity anomaly at ~5 km depth beneath central Tenerife, interpreted as a phonolitic magma reservoir [Koulakov et al. 2023], which suggests that similar heightened volcanic activity may also be a risk in this region. Understanding how petrological data reflect magmatic processes can be used and integrated with other monitoring data including geophysical parameters and gas geochemistry during volcanic crises [Re et al. 2021]. This would lead to development of enhanced risk assessments, enabling more informed decisions regarding the mitigation of potential hazards and the protection of lives and properties. For example: X-ray micro-computed tomography can rapidly characterise the composition of natural olivine crystals in erupted basalts permitting tracking of changes in magma components that control the evolution of an eruptive system [Pankhurst et al. 2014]; variations in whole-rock major element compositions provide insights into changes in magma temperature and thus viscosity affecting lava flow patterns [e.g. Gansecki et al. 2019]; diffusion chronometry results can reveal varying ascent rates influenced by crystallisation characteristics that may affect eruption style [Kahl et al. 2022]; and, variations in major and trace elements glass compositions—determined by scanning electron microscope energy dispersive X-ray spectroscopy—may be linked to transitions from more primitive to evolved magmas, resulting in changes in eruptive explosivity and frequency that can inform hazard assessment [Corsaro et al. 2024].

Here, clear temporal variations are identified in whole-rock data of the 2021 Tajogaite eruption that permit division of the activity into 3 stages: initiating, tapping-evacuating, and waning. First, we consider how the compositional variation may have been generated then how the range of compositions were extracted and erupted. In this way a petrogenetic model is developed below that links magma system structure, pre-eruptive processes and syn-eruptive behaviour to changes in both the compositions of the eruptive product and eruption dynamics. These findings provide valuable insights into the Tajogaite eruption and are more broadly applicable to other volcanoes such as Kīlauea 2018 and Fagradalsfjall 2021 (see below: Section 7.3: Harnessing the full potential of petrological monitoring: lessons from recent mafic eruptions).

7.1 Generation of the compositional variations—magmatic processes

A range of processes may play a role in the compositional evolution of the lavas and tephras: primary variations resulting from tapping of heterogeneous mantle sources and variable degree mantle melting over a range of depths; as well as secondary differentiation from fractional crystallisation, magma mixing, contaminant assimilation, and filter pressing of residual melt. Such processes defined the character and controlled the evolution of historic eruptions on La Palma [e.g. Klügel et al. 2000; Barker et al. 2015]. With the benefit of multidisciplinary datasets, we assess the relative importance of each and how they contributed to temporal trends during the Tajogaite eruption.

7.1.1 *Mantle homogeneity*

The majority of the lavas exhibit coherent and consistent compositional characteristics (Figures 3–6), the implication being that the mantle source was invariant. In agreement with this, Day et al. [2022] concluded there was no reason to suggest mantle source heterogeneity.

During active eruptions the distinction between magma batches and magma pulses is relevant when interpreting geophysical and geochemical signals of magma system dynamics to forecast eruption evolution and assess hazards. Batches represent compositionally distinct, spatially and temporally constrained volumes of discrete emplacement from different sources [Zellmer and Annen 2008]; whereas pulses may be considered as episodic or ephemeral movements of magma, derived from the same source, into or through an intrusive or volcanic system.

Potential magma source heterogeneity may be assessed further by considering variations in whole-rock incompatible element ratios. In recent eruptions from Fagradalsfjall, Iceland, and Hawai'i, variations in whole-rock lavas K_2O/TiO_2 ratio of 0.2 and 0.16, respectively, are interpreted to reflect tapping of heterogenous mantle sources [Gansecki et al. 2019; Bindeman et al. 2022]. Conversely, excluding the mineralogically complex Stage 1, the K_2O/TiO_2 of the Tajogaite lavas and tephras presented here only varies by 0.09 across the whole eruption (Figure 5K). Similarly, Nb/Zr varies by 0.16 over the first 60 days of the 2021 Icelandic eruption, again attributed to variation in distinct mantle source components; however, it only changes by 0.02 in the Tajogaite lavas (Figure 6L).

Our whole-rock data inference that the mantle source was homogeneous is supported by constant atmospheric-contamination-corrected $^{3}He/^{4}He$ values in olivine- and clinopyroxene-hosted fluid inclusion throughout the eruption [Sandoval-Velasquez et al. 2023], and uniformly high CO_2/SO_2 ratios from the lava-fountaining vents [Burton et al. 2023].

Ubide et al. [2023], however, invoked tapping of distinct magma batches to explain variations in radiogenic groundmass $^{87}Sr/^{86}Sr$ ratios. Initial values in their Phase 1 dropped through Phase 2 then diversified from Phase 3 onwards, albeit with values mostly overlapping, into highly radiogenic and unradiogenic (their Figure 2). However, a lack of significant changes in the lava and tephra major and trace elements related with the Sr isotope variations is also consistent with assimilation of crustal material, which fits with heterogeneity in radiogenic $^{187}Os/^{188}Os$ during Stage 1 and early Stage 2 [Day et al. 2022]. See discussion in Section *7.1.4*: Assimilation, below.

It thus appears likely that Tajogaite erupted episodic magma pulses from a single mantle source (with small but variable degrees of crustal assimilation) rather than distinct magma batches. Accordingly, Charco et al. [2024] concluded quasi-exponential ground surface deflation likely reflected a pressure drop in the magmatic system consistent with mass conservation, which indicated no new influxes of magma occurred during the eruption period and allowed for hindcasting of the end of the surface expression of the magmatic activity.

7.1.2 *Mantle melting*

All Tajogaite lavas and tephras exhibit elevated light REE to heavy REE ratios (La_N/Yb_N 22.4–25.3, only varying by ~0.3) and middle REE to heavy REE (Dy_N/Yb_N varying by 2.0–2.2). The consistency and simplicity of these inclined patterns (Figure 4B) indicates a broadly uniform low degree of partial melting of a single mantle source, which is in agreement with conclusions of Day et al. [2022]. The degree of melting, and source, can be modelled as ~1–2 % of a garnet-spinel-bearing (80–60 km) region of enriched mantle (Supplementary Material 2) considerably deeper than thermobarometric estimates of mineral crystallisation. Similarly, Day et al. [2022] proposed 2.5–3.0 % partial melting of a fertile garnet-bearing asthenospheric source. The Tajogaite source depth results are consistent with mantle melting calculations for the 1949 eruption during which primary melts apparently ascended from a garnet-bearing deep, 80–100 km, source [Klügel et al. 2000].

7.1.3 *Fractional crystallisation*

The lava and tephra whole-rock MgO content <9 wt.% and olivine forsterite content <90 imply some degree of evolution from primary magmas [Day et al. 2022; Pankhurst et al. 2022; Dayton et al. 2023] consistent with geophysical evidence for an extensive magmatic system [D'Auria et al. 2022] and thermobarometric calculations that record a range of migration-, ponding-, and differentiation-related crystallisation depths for the 2021 eruption [Castro and Feisel 2022; Dayton et al. 2023; Fabbrizio et al. 2023; Sandoval-Velasquez et al. 2023; Ubide et al. 2023; Zanon et al. 2024] and La Palma as a whole [Klügel et al. 2005].

Compositional variation was modelled using the `Magma Chamber Simulator` software [Bohrson et al. 2020, Supplementary Material 3], which confirmed clinopyroxene was the liquidus phase at temperatures of 1290–1260 °C at 7 kbar (~24.5 km below ground level; fO_2 NNO). During Stage 1, Mg and other elements (Figures 5 and 6) show limited ranges, consistent with a small reduction in magma temperature (1263–1233 °C) driving crystallisation and fractionation of clinopyroxene with a composition comparable to measured mineral chemistry [cf. Pankhurst et al. 2022] and minor apatite (Supplementary Material 3). In the same way, crystallisation of clinopyroxene over a narrow temperature range (~1290–1245 °C) reproduced the Stage 2 elemental ranges without the need for more complex modelling (Supplementary Material 3). However, it should be noted plotting macrocryst compositions relative to the dataset revealed a role for ~20 % olivine in the fractionating assemblage together with clinopyroxene rim compositions (Figure 4A). The abundances of TiO_2 and P_2O_5 were controlled by oxide and apatite fractionation, respectively (Supplementary Material 3).

We suggest the Tajogaite magmatic system was compositionally zoned prior to eruption onset because: i) discrete magma pulses were inferred from the occurrence of seismic swarms and gas flux changes throughout the decade prior to eruption onset [Padrón et al. 2022]; ii) magma storage calculations describe crystallisation as occurring across a considerable depth interval in the upper mantle and lower crust (see Section 6.2: Magma storage conditions, thermobarometry, and calculations, above) and such a system is unlikely to be fully connected and mixed; iii) the rate of change in whole-rock lava elemental compositions through Stage 2 is of the same order as that through Stage 3, just in a different direction (Figures 5 and 6); and iv) the range of compositions erupted over a short time scale would require both cooling and efficient crystal settling for which there is no evidence at present, most notably towards the end of the eruption. Evolution of a parental magma composition by fractionation occurs as time progresses, so this process could only be responsible for the Stage 2 temporal trend to more primitive composition if those compositional variations were already present across the plumbing system. Hence, by Stage 2 the plumbing system must have contained different compositions which, regardless of degree of mixing, erupted in a manner and rate that preserves at least some of the variation present. Therefore, there is no need to invoke active syn-eruptive fractionation to explain the Stage 3 trend, even though the compositional changes over time are to more evolved.

7.1.4 *Assimilation*

Physical evidence of assimilation is observed in the current study: variably resorbed amphibole, its reaction products, and biotite in the Stage 1 rocks; rare, yet consistently present, specks of xeno-pumices in the Tajogaite lavas and tephra (cf. the El Hierro 2011 eruption [Meletlidis et al. 2012]); as well ultramafic and gabbroic micro-xenoliths. Moreover, compositional evidence of mixing is inferred from isotopic data. Day et al. [2022] reported distinct lava whole-rock Os concentrations and $^{187}Os/^{188}Os$ between lava samples, which they interpreted as interaction between a low concentration Os and radiogenic source and a higher concentration, less radiogenic, one. Ubide et al. [2023] described variable $^{87}Sr/^{86}Sr$ within groundmass, yet observe no correlation between Sr, MgO, or SiO_2; although, this does not rule out the Sr-radiogenic signatures being the result of crustal contamination if the assimilant is hydrothermally altered basic oceanic crust [White and Klein 2014].

In general, the early erupted lavas and tephra are both more evolved and radiogenic than the later ones and temporal trends emerge that broadly correlate with chemical composition and stages. Osmium concentrations were least abundant and $^{187}Os/^{188}Os$ most radiogenic at the start of Stage 1, then trended to the highest elemental concentrations and least radiogenic isotopic compositions into Stage 2 Day et al. [2022]. Two of the four analysed Stage 2 lavas have anomalously low $^{187}Os/^{188}Os$ values attributed to non-systematic anthropogenic pollutants leading to them being disregarded from consideration. The remaining Stage 2 $^{187}Os/^{188}Os$ analyses are higher than the mode, raising the question of whether Stage 3 lavas might continue the trend to lower Os concentrations and more radiogenic $^{187}Os/^{188}Os$, but data are not available for Stage 3. Ubide et al. [2023] observed that the groundmass had radiogenic $^{87}Sr/^{86}Sr$ ratios in their Phase 1 which decreased through Phase 2 and then from the start of Phase 3 onwards split into two trends, radiogenic and unradiogenic through time, albeit with values mostly overlapping (their Figure 2). Both studies found their isotopic data to be consistent with minor assimilation of comparatively radiogenic sedimentary and/or volcanic materials occurring during magma ascent. However, Ubide et al. [2023] favoured tapping of magma from distinct sources during the eruption, whereas varying degrees of crustal assimilation into a relatively homogeneous magmatic source was suggested by Day et al. [2022].

Notably, wall rock assimilation was considered an important process in the evolution of the 1949 basanite magmas [Klügel et al. 2000], whereas the 1971 lavas indicated assimilation of deeper levels of the magmatic system including leucogabbros and kaersutite cumulates [Barker et al. 2015].

7.1.5 *Filter pressing of residual melt*

Consideration of a further mechanism to generate the observed time series compositional variations was motivated by comparing compositions of tephra glass Longpré et al. [2024] and the whole-rock lava. A close match in parallel trends is observed in silicate- and phosphate-forming elements until the beginning of Stage 3, when they become strikingly decoupled (Figures 5 and 6). Tephra glass compositions change in step with the lava whole-rock compositions, yet much more strikingly, for CaO, Na_2O, K_2O, and P_2O_5, and more moderately for SiO_2. Stage 3 lava whole-rock compositions form an array on a modelled fractionation from Stage 2, yet active fractionation need not be invoked (see Section *7.1.3*: Fractional crystallisation, above) and, in the time available, would not result in such extreme compositions. Rather, the progressive change in measured melt composition accounts for the trend observed in the whole-rock lavas without any change required in the crystal cargo. The largely invariant macrocryst proportions, ~17 area%, in Stage 2 and Stage 3 (Table 1) demonstrates that indeed these minerals cannot be responsible for the Stage 3 whole-rock compositional variation. As a comparison, Bindeman et al. [2022] concluded the compositional variation in the 2021 Fagradalsfjall lavas from Iceland was not attributable to mineral proportions because macrocrysts only varied from 2–15 modal%.

Changing the melt composition so drastically without varying the modal proportions of mineral phases requires either assimilation of a significant proportion of crystal-poor yet evolved melt, or some readily fusible and highly evolved assimilant whose composition is on the same fractionation path. There is no indication that the volume of, albeit SiO_2-rich, clinopyroxene- and olivine-free, xeno-pumice assimilated is sufficient to account for the degree and direction of melt composition change. This leads us to hypothesise that a progressively greater participation of residual melt, stored in fractionated lenses of magma with higher crystal content than the erupted magmas and extracted by deformation- and gas-driven filter pressing, provides a potential solution.

7.2 Eruption of the compositional variations—dynamic processes

An opportunity to explore the physical driving factor(s) modulating the eruption is provided by our temporally well-constrained sequence of lava and tephra samples, placed into the context of the mechanisms that explain their compositions together with complementary time-series petrological

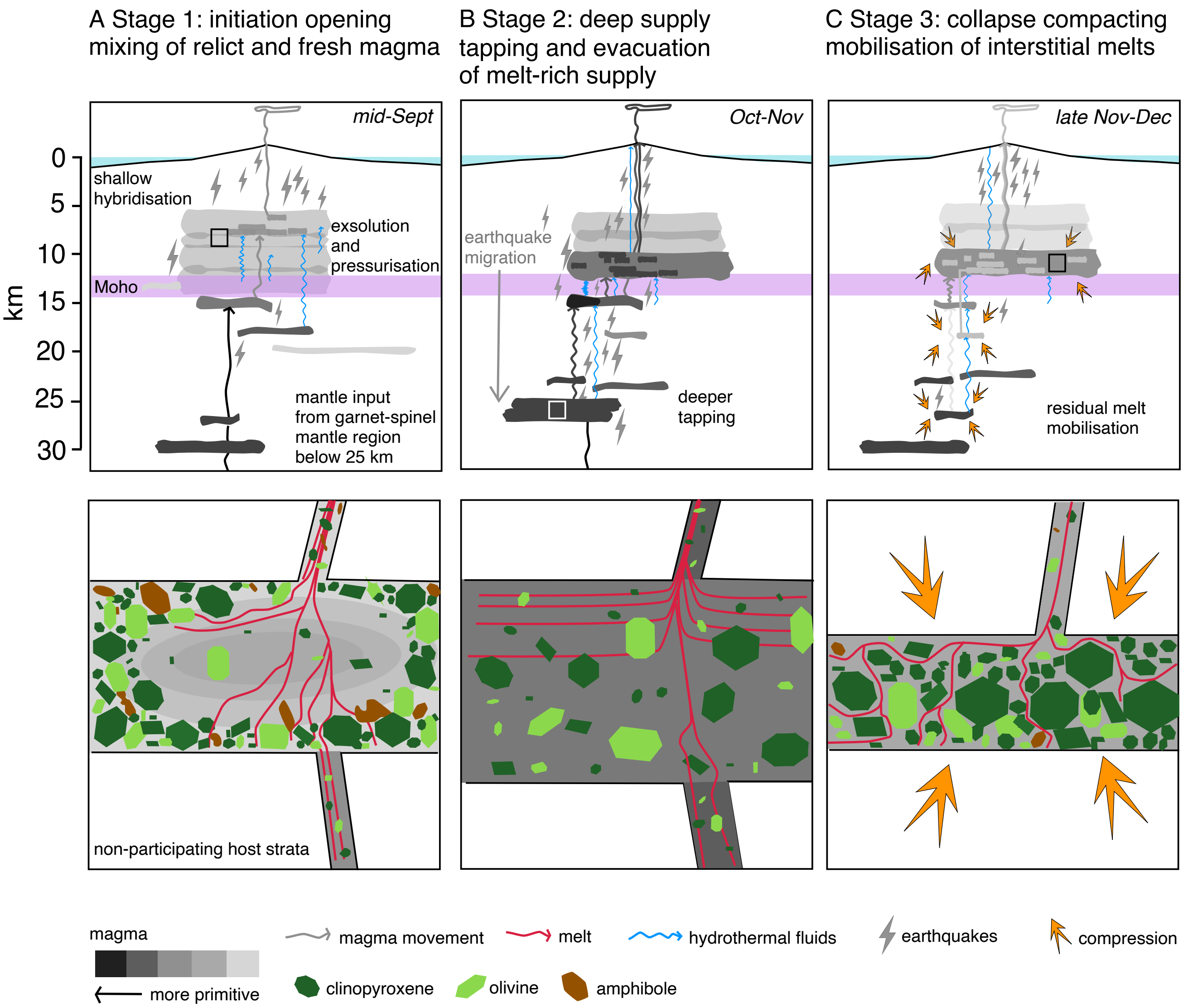

Figure 7: Schematic diagram of magmatic system evolution and physical controls on lava composition. [A] A shallow magma body was mobilised in the days prior to September 19th as a conduit opened to the surface. [B] Release of magma from progressively deeper levels in the mantle reservoir reached a relatively steady state that continued for two months. [C] Evacuation finally led to progressive collapse and compaction of magma lenses, reflected in ground surface deflation, increasing extraction and greater relative contribution to the lava of less easily mobilised interstitial melt from crystal mush. Boxes in each top figure mark the locations of the magma systems shown in the lower panels.

data [Day et al. 2022; Sandoval-Velasquez et al. 2023; Ubide et al. 2023; Zanon et al. 2024]. The benefit of time-stamped sampling allows construction of a causative model (Figure 7) based upon key premises in igneous petrology: i) fractionation occurs by physical separation of melt from crystals [Hildreth 1981; Hu et al. 2022]; ii) crystal-poor magmas flow more freely than crystal-rich magmas of the same composition [Marsh 1981; Frontoni et al. 2022]; and, iii) melt residual to crystallisation is more evolved than the bulk composition of the initial magma [Bowen 1928; Portner et al. 2022]. Manifestly, the mush component of magmatic systems influences the mechanical, thermal, and chemical evolution of igneous processes [e.g. Cashman et al. 2017; Lissenberg et al. 2019; Liao 2022].

The time between magma provoking unrest as a result of its migration and/or accumulation at depth(s) to its eruption requires consideration of temporal shifts to interpret petrological data and compare it with other monitoring data such as seismicity (Figure 8). For example, applying microthermometric analysis of fluid inclusions in crystals by determining the temperatures of phase changes during heating and cooling to estimate depths and ascent velocities Zanon et al. [2024] described an acceleration from traversing tens of kilometres in depth in weeks to days, before traversing the final 5 to 10 km in hours. Furthermore, rapid magma ascent, 10 km over ~7 days, was also indicated by seismicity that migrated rapidly towards the surface over a period of 7 days, moving along structural weaknesses marked by low-velocity tomographic anomalies

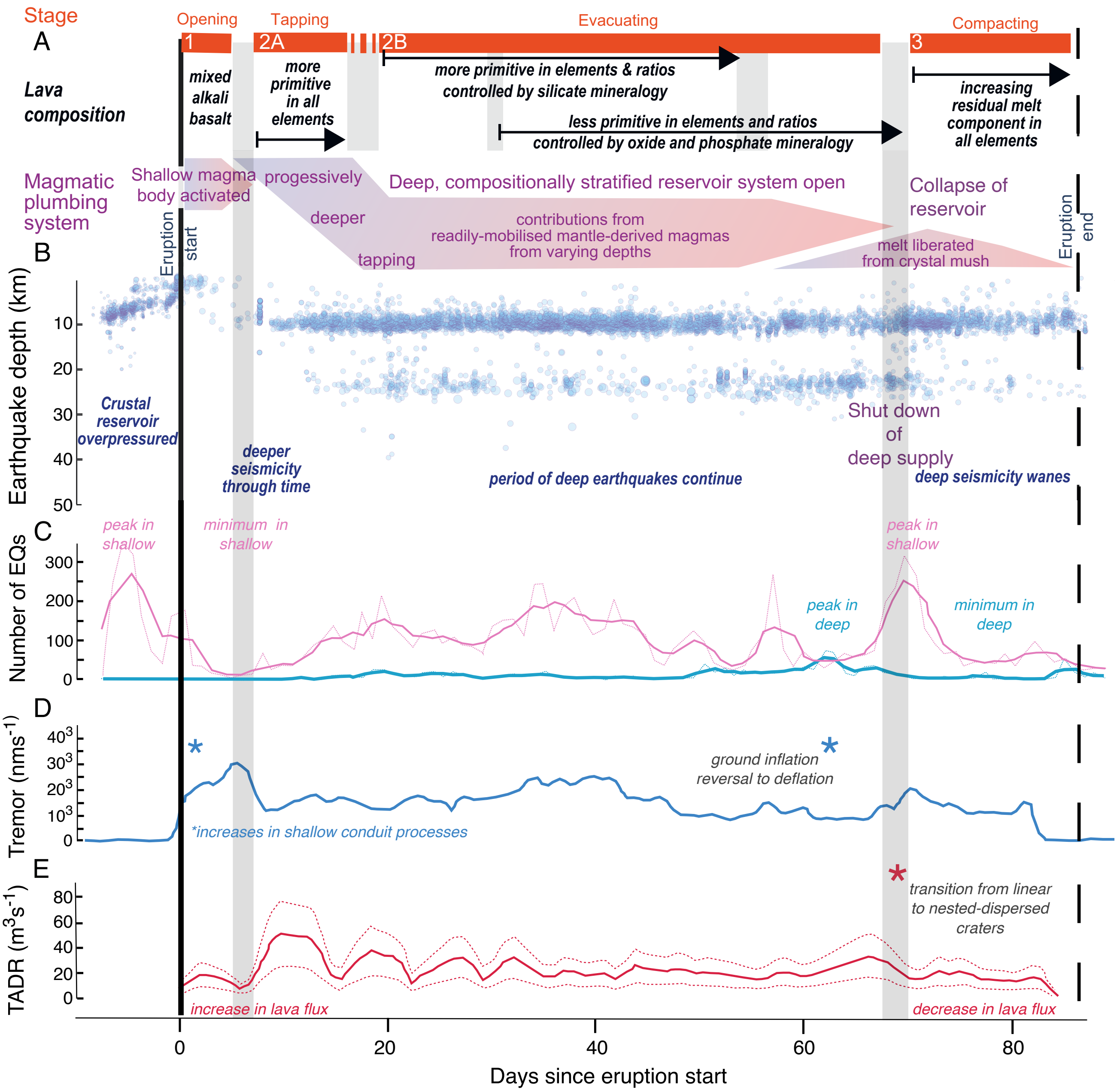

Figure 8: Magma plumbing system processes interpreted from trends in lava compositions through time and compared with real-time seismicity. [A] Alkali basalt contaminated with material from previous magmatic events is erupted initially and defines Stage 1. A progression to more primitive and pristine alkali magma follows and defines Stage 2A, the end of which is indicated by the lowest Ti, P, and incompatible trace element concentrations measured. Stage 2B is defined by a protracted period of subtle compositional changes indicating comparatively passive evacuation of reservoirs, which ends at a sharper deviation or inflection in most major and minor elements. The final trend, Stage 3, is most simply interpreted as fractionated Stage 2B magma and indicates increasing contributions of residual melt from zones of higher crystallinity from the same reservoirs. [B]–[D] Causative links can be drawn between lava composition and seismological records (data from Government Report [2022], D'Auria et al. [2022], and Charco et al. [2024]). [E] Time-averaged lava discharge rate (TADR) and change of crater orientation (data from Bonadonna et al. [2022] and Muñoz et al. [2022]). Key magma system processes are recorded simultaneously across each dataset.

[D'Auria et al. 2022]. A single time correction is clearly not appropriate because of multi-component sourcing from different depths and potential lack of synchronicity between magmatic processes, their geophysical signals, and release of erupted materials. Nevertheless, such estimations of timescales provide an important framework for assessing the significance of any pattern observed between erupted products and real-time signals of magma movement. A case for aligning compositional variation of the erupted melt and geophysical data is explored in Longpré et al. [2024] and future crystal-scale studies including integration of diffusion chronometry and melt- and fluid-inclusion barometry will refine how this challenge is addressed.

7.2.1 *Stage 1—triggering of crystal mush, deep magma input, and gas overpressure*

Deep-sourced magma input driving magma buoyancy and overpressure by exsolved gases 7–25 km beneath Cumbre Vieja (cf. Kīlauea [Gansecki et al. 2019]; Etna [Corsaro and Miraglia 2022]) most likely led to the rapid ascent of magma pooled at the base of the crust, ~10 km [D'Auria et al. 2022; Padrón et al. 2022; Zanon et al. 2024]. Eruption triggering culminated in lava fountaining and explosive activity from central upper vents along with spattering and lava effusion from flank vents. Related to this, volcanic tremor, which reflects shallow conduit processes [Eibl et al. 2023], was non-existent prior to the eruption, then increased dramatically through Stage 1 [Figure 8D; D'Auria et al. 2022].

Flux of hot primitive magma into more evolved magma systems can result in compositional heterogeneity, crystal resorption and reverse zoning [Bowen 1928; Ubide et al. 2021], as visible in the Tajogaite eruptive products (Figure 3C). Textural evidence from Stage 1 rocks also indicates amphibole, most likely remnants of a residual magma from previous eruption(s), was transforming and resorbing (Figure 3C), which would have contributed additional volatiles, in particular H_2O, to the magma, the extent and effects of which are currently being assessed. These petrographic observations, and comparatively broad ranges of whole-rock and glass (melt) major elements such as SiO_2, CaO, and FeO erupted during Stage 1 are particularly indicative of pre-existing magmatic heterogeneity. The heterogeneity is in accordance with the magmatic system opening its passage to the surface related to deep-sourced magma input (Figures 5 and 6), and consistent with detection of fluids ascending ahead of the main magma dyking [Cabrera Pérez et al. 2022]. These processes mobilised a relatively evolved and hydrous 'stagnant' crystal-rich magma, or mush, that recorded shallow residence in the middle to lower ocean crust and top of the mantle, 6–16 km [Figure 7A; Romero et al. 2022; Fabbrizio et al. 2023; Ubide et al. 2023; Bonechi et al. 2024; Zanon et al. 2024]. Mixing would have resulted as recorded in the zoned clinopyroxene macrocrysts and the mush most likely contained ante and/or xenocrystic material: vestiges from previous magmatism, perhaps including the 1949 event that occurred in the same region (Figure 1A); and remnants of non-eruptive magmatic events from the years preceding 2021 [cf. Zanon et al. 2024]. Day et al. [2022] proposed the Stage 1 magma was emplaced between four to ten years prior to the eruption on the basis of magmatic unrest reflected in seismic detection, gas monitoring and geodetic surveys. Accordingly, the Os and Sr isotopic data [Day et al. 2022; Ubide et al. 2023] record a compositional effect of contamination most noticeably during Stage 1 when volcanic activity was initiating.

7.2.2 *Stage 2—evacuation of deep, primitive, and variably fractionated, mobile magmas*

The transition from Stage 1 to Stage 2A coincided with a progression of seismicity down to ~25 km (Figure 8), with some evidence for magma movement as deep as 40 km [Castro and Feisel 2022; Romero et al. 2022; Fabbrizio et al. 2023; Ubide et al. 2023; Bonechi et al. 2024]. Bottom-up triggered perturbation led to top-down propagation which facilitated access of the primitive and readily mobilised portions of the magmatic system to the active feeder structures. As the system completed its opening phase to greater depths, a minimum in shallow earthquake frequency and a drop from peak volcanic tremor signalled a more open conduit and passage (Figure 7B). In agreement with a more open conduit assimilation of contaminant was less evident in the Os and Sr isotope data during this stage [Day et al. 2022; Ubide et al. 2023] because, we suggest, minor components were swamped by free-flowing mantle-melt dominated magma.

During the transition to deeper seismicity, olivine- and clinopyroxene-hosted fluid inclusion He-CO_2-N_2 concentrations increased [Sandoval-Velasquez et al. 2023; Zanon et al. 2024]; these time series variations in magmatic volatiles were attributed to tapping of magma from a more primitive, deeper, less-degassed reservoir. A deeper, more volatile-rich source is consistent with eruption of more mafic magma characterised by greater olivine forsterite content and a ~two-week trend to higher whole-rock MgO, CaO/Al_2O_3, Ni, and Cr concentrations (Figures 5 and 6 [cf. Day et al. 2022; Ubide et al. 2023; Zanon et al. 2024]). Associated with the more primitive lava, discharge rate more than doubled over this period [Figure 8E; Bonadonna et al. 2022] as the hotter, less viscous, more primitive magma erupted (Figure 5). Notably, similar changes in eruptive style were also observed one week into the Kīlauea 2018 eruption [Gansecki et al. 2019]. Furthermore, through Stage 2 the arrangement of craters became more dispersed [Muñoz et al. 2022].

Tapping of progressively less-evolved composition was linked by fractional crystallisation of clinopyroxene (Supplementary Material 3), a process also evidenced in glass compositions. Plateauing of increases in MgO, Ni, and Cr (Figures 5A and 6A–6B) coeval with a flattening out of decreases in Al_2O_3, TiO_2, P_2O_5, Sr, and REEs (Figures 5 and 6) reflects the Stage 2A to 2B shift to more steady-state deep magma extraction. As a result, a period of relatively uniform frequency, bimodal depth, seismic activity ensued centred at ~25 km and ~12 km (Figure 7; Figure 8B–8C). By contrast, CaO, FeO, and Sc concentrations increased continuously through Stage 2 (Figures 5C–5D and Figure 6D) which is consistent with erupted compositions recording the extraction of magmas that had experienced slightly increasing degrees of clinopyroxene crystallisation. The effect of oxides on melt compositions is more clearly delineated by increases and decreases in the glass FeO and TiO_2 values (Figure 5).

Gradual waning of the discharge rate was observed through Stage 2 until around day 60 [Bonadonna et al. 2022] which was linked, we conclude, to an exhaustion of the deep mantle-derived, MgO-rich, magma supply which is in agreement with suggestions that the supply diminished from late November onwards [Day et al. 2022; Zanon et al. 2024]. A few days before the Stage 2–3 transition commenced a significant peak in deep earthquakes was observed at day 63, then the focus of seismicity shallowed from ~25 to ~10 km [D'Auria et al. 2022, Figure 8]; and compaction of the magma system was inferred from detailed seismicity studies [Charco et al. 2024].

7.2.3 *Stage 3—filter pressing of less mobile melts*

The pre-Stage 2–3 transition peak in deep earthquakes was followed by a significant peak in shallow earthquakes around a week later (~day 70) (Figure 8C). Volcanic tremor also peaked once more just days after Stage 3 began [D'Auria et al. 2022] indicative, like the earthquake data, of a shift in the focus of magmatic activity to a shallow level (Figure 8D). This sequence coincided with a subtle increase in lava discharge rate before it finally decreased again (Figure 8E). The shallow seismicity subsequently declined through Stage 3 (Figure 8B–8C) and a significant shift occurred in crater alignment from broadly linear to more distributed, nested-dispersed [Muñoz et al. 2022]. However, thermobarometric records of crystallisation depth ranges did not change across the stage transition, indicating the magma tapped by the deep pathways were still sampled from the shallower levels (see Section 6.2: Magma storage conditions, thermobarometry, and calculations).

Disaggregation of crystal mush zones is an effective mechanism for extracting more evolved interstitial melt in a dominantly mafic context [Costa et al. 2010; Passmore et al. 2012] with pressure-driven melt extraction, equivalent to a natural deformation-driven process, numerically modelled to occur over short (weeks to months) timescales [Wong and Keller 2023]. Melt segregation and transport rates depend on source material permeability, compaction process, and the number, size, and connectivity of contributing lenses.

However, when evaluating melt segregation and extraction using existing models and/or experimental findings in light of the ascent rates reported in Section 6.3: Magma ascent rates, it should be borne in mind that the filter pressing process does not need to transport the melt to the surface. Rather, it is enough for less mobile, more evolved, viscous melt from mush lenses to be displaced sufficiently for it to be incorporated into the already active ascending magma system. Notably, earthquake travel-time seismic tomography indicated magma ascent rates of 10–12 km over a period of seven days at the beginning of the eruption [D'Auria et al. 2022] with fluid inclusion results indicating similar rates [Zanon et al. 2024]; microlite number density and crystal size distribution ascent rate estimates, on the other hand, were up to three times faster [Romero et al. 2022; Bonechi et al. 2024].

A 2D model of centrifuge-driven porous-media channeling instabilities of basalt melt flow through olivine aggregates with porosities of 5–12 %, which reflects natural density-driven scenarios, yielded maximum melt displacement of several meters over two weeks [Connolly et al. 2009]. Significantly, permeability beneath Tajogiate was most likely higher during the first two stages of the eruption. D'Auria et al. [2022] concluded that high P wave/S wave velocity ratios and low S wave velocities indicated "a considerable amount of partially molten material in the sub-crustal region" although melt percentage was not quantified.

In addition, it is important to take into account that deformation-driven compaction will distort and most likely enhance extraction rates modelled for density-driven filter pressing melt. As a counterpoint to the generally accepted association between injection of magma into a system and pressurisation [e.g. Ewart et al. 1991; Wadge et al. 2006; Chang et al. 2007] deep magma supply shutdown, such as we propose for Tajogaite, could reduce the internal pressure and buoyancy of the magmatic system [Papale et al. 2017]. In this way, gravity and lithostatic pressures would enhance compaction as apparently recorded by transient, accelerated contraction in ground deformation noted by Charco et al. [2024] (Figure 8D). Considering mantle deformation-driven melt extraction, Katz et al. [2022] concluded that melt movement rate and direction were influenced by alignment and growth of shear-driven melt bands. Deformation increased melt extraction transport rates to metres over two weeks, significantly exceeding the millimeter-scale displacement predicted for simple diffuse porous flow. Similarly, starting from a melt-rich environment with an initial composition of 30 % crystals and 70 % melt, Schmidt et al. [2012] modelled melt expulsion from a cumulate layer by gravitational settling-driven compaction. They calculated that mechanical compaction could reduce the porosity to 30 % in a 50-meter-high olivine cumulate pile in significantly less time than the one to seven days estimated for slower chemical compaction. Furthermore, channelised flow within mushes, such as suggested for the Tajogaite magma system [D'Auria et al. 2022], segregates melt more efficiently than porous flow [Marsh 1981; Lissenberg et al. 2019] and facilitates crystal entrainment. Hence, this could explain the detection of different macrocrysts in the Stage 3 magma, such as the eruption of olivine hosting both deep, N2-bearing, and shallow, N2-free, fluid inclusions [Zanon et al. 2024] and, to date, a single example of reappearance of xeno/antecrystic amphibole.

In conjunction with compaction-driven and channelised mechanisms, gas-driven filter pressing is an effective process to expel fractionated melt from crystal mush in shallow magmatic systems, <10 km; gas effervescence creates a strong pressure gradient mobilising residual liquids [Anderson Jr et al. 1984; Sisson and Bacon 1999; Pistone et al. 2015]. For instance, Pistone et al. [2015] calculated extraction and transport velocities of 0.05–0.5 $m\,yr^{-1}$ for a melt fraction of 0.4 in an experimental setting with dacitic composition, extrapolating these results to reach up to 11 $m\,yr^{-1}$ in natural silicic systems. Notably, a high gas content in the magmatic system was evident throughout the Tajogaite eruption, even in its final stages: the central upper fountaining vents emitted consistently high CO_2/SO_2 gas ratios [Burton et al. 2023]; strong explosive activity on the last day of the eruption ejected bombs and produced gas-and-ash plumes; and intense emissions persisted even beyond the end of lava emission [GVP 2022].

In short, it was only in the final stage of the eruption, just before Stage 3 commenced, that the shutdown of the deep, mantle-derived, MgO-rich, magma supply led to large-scale collapse of the gas-rich magmatic plumbing system. Consequently, compaction-related, deformation- and gas-driven, filter pressing process, related to lithostatic load and shear compaction which can result in rapid separation of melt from previously untapped low permeability connected mush lenses [cf. Komar 1972; McKenzie 1984; Natland and Dick 2001; Petford et al. 2020] began to enhance the mobilisation and release of more evolved [Longpré et al. 2024], higher viscosity [Soldati et al. 2024], less mobile residual melt fractions from the interstices of crystal-rich magma lenses. The extracted melt became an increasingly abundant entrained component of the ascending magma, accounting for the Stage 3 decoupling of magma and melt—which changed—and the crystal components—which remained unchanged. This process represents a compelling mechanism that heralds the end of the eruption and reconciles petrological signals that are otherwise difficult to explain.

Without the benefit of the tephra glass data, it had been suggested that syn-eruptive fractional crystallisation was the driving mechanism for the final compositional changes and eruption cessation [Ubide et al. 2023]. However, systematic description and near-daily sampling of continuously hybrid explosive-effusive volcanic eruptions are rare, limiting opportunities to compare time-series data from simultaneous lava and tephra. Therefore, it is worthwhile exploring other signals in the Tajogaite eruptive products that might clarify the roles of fractional crystallisation and residual melt participation in signalling eruption cessation.

In this context, it becomes even more critical to assess the timescales of processes thoroughly. In a study of clinopyroxene crystallisation in mafic alkaline magmas, Zhou et al. [2021] emphasised that mineral growth rate can depend upon the degree of undercooling [cf. Mollo and Hammer 2017]. At small degrees of undercooling crystals grow more slowly in near chemical and textural equilibrium resulting in euhedral morphologies. By contrast, rapid nucleation and growth occurs when undercooling is greater, leading to sub-anhedral morphologies including skeletal and dendritic forms. The petrographic textures of the Stage 3 Tajogaite lavas (Figure 3G–3H) indicate the former, gradual crystallisation, a scenario that would not favour short-duration differentiation by mineral fractionation. Moreover, olivine crystals in the Icelandic 2010 Eyjafjallajökull eruption products, also alkali basalts with similar magmatic temperatures, grew only 30–50 μm rims on pre-existing crystals over a period of two to three weeks prior to initiation of the eruption [Viccaro et al. 2016], despite inferences that growth was enhanced by mafic magma injection. Furthermore, it is important to consider that mineral segregation will be impeded by any turbulence within the magmatic system [Huppert and Sparks 1981].

Crystal segregation from melt is a function of grain size: the critical crystal size above which fractional crystallisation of common silicate minerals occurs by crystal segregation from a basic magma is estimated to be around 1 mm [Solomatov 2007]. Given the above growth rates, some five months would be needed for crystal growth to a point where phases could efficiently fractionate. Strikingly, and by contrast, in historical eruptions of the Icelandic Eastern Volcanic Zone Bárðarbunga-Veiðivötn volcanic system, melt was extracted and erupted from subvolcanic mush over periods as short as two weeks [Hartley et al. 2016; Neave et al. 2017; Caracciolo et al. 2021].

A fresh pulse of deep magma could reverse a Stage 3 type trend. If the magma intrusion was breaking through fragile crust this should be indicated, almost in real-time, by changes in the nature and increased frequency of deep earthquakes. That said, if the newer intrusions ascended through recently formed, previously active, pathways unrest could be masked and renewed activity aseismic. Despite that, the composition of subsequently erupted lavas and tephra should highlight the reactivation, thus further emphasising the importance of near-real-time petrological monitoring.

In summary, we propose a straightforward progression of initiation and shallow evacuation → primitive magma emptying → exhaustion → compression and residual melt participation → final feeder structure closure and eruption end, a causative order that tracks increasingly less eruptible magma over time (Figure 7C).

7.3 Harnessing the full potential of petrological monitoring: lessons from recent mafic eruptions

Real-time forecasting using petrological insights gleaned from volcanic deposit compositions is challenging because of the paucity of comprehensive, time-constrained, data. However, recent petrological time series studies have potential to significantly advance understanding of processes and signals across sub-disciplines and allow for rapid interpretation of generated data. In this respect it is worth noting that lava and tephra compositions overlap in the main stages of the Tajogaite eruption (Figures 5 and 6). Therefore, it is apparently valid to time series sample continuously deposited tephra to assess magma compositions as an alternative to accessing lava flow fronts should the latter prove logistically complicated.

Another challenge in using petrological monitoring data is the establishment of workflows for rapid sample processing [Re et al. 2021]. Yet, where appropriate analytical infrastructure exists and a sound understanding of the magmatic systems is available, there are examples of petrological monitoring having been used during eruption response. During the 2018 Hawaiian eruption, Gansecki et al. [2019] undertook syn-eruptive, short-term, forecasting using near-real-time rapid energy dispersive X-ray spectroscopy geochemical analysis of lava, providing critical information for hazard assessments. In particular, they informed authorities about the eruption and flow of more primitive, hotter, less viscous lava, enabling an effective and efficient response to changes in eruptive style.

As described and interpreted above, our new results identify changes in compositional trends of whole-rock and glass data to more evolved compositions some two weeks before the eruption ended (Figures 5 and 6). Using these data we hindcast the beginning of the end of the Tajogaite volcanic activity

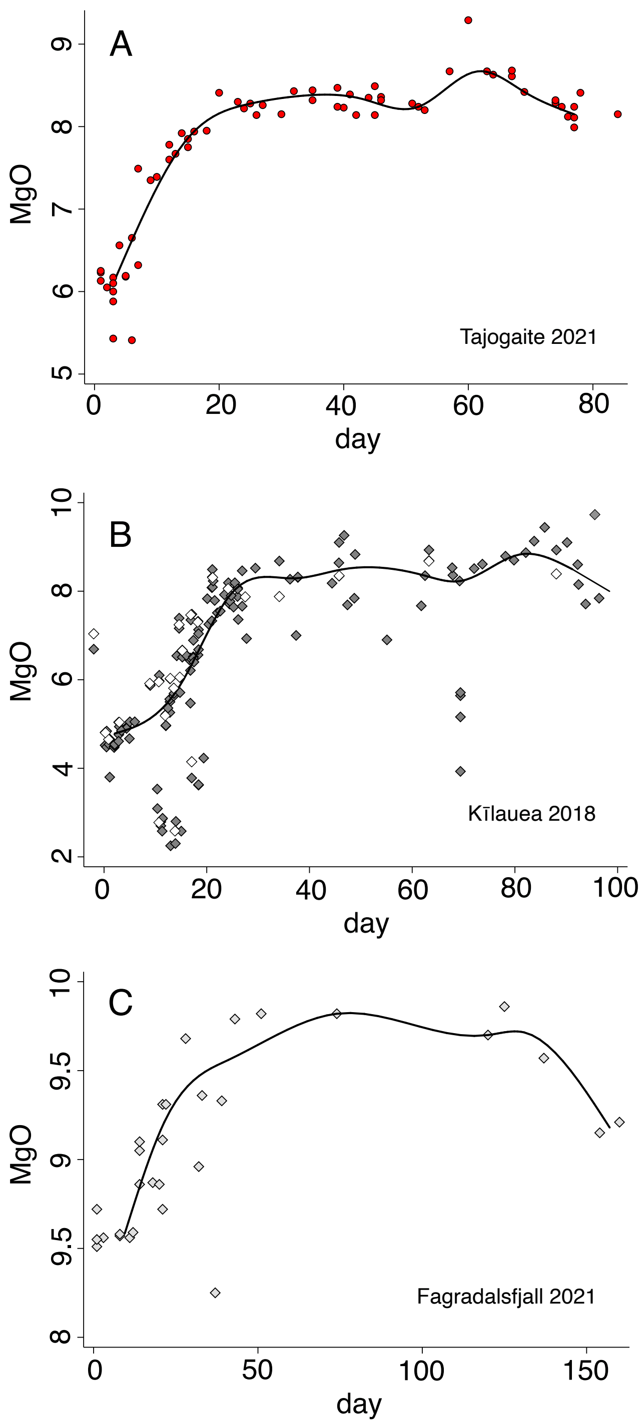

Figure 9: Across-eruption time series variation in MgO for three recent mafic eruptions. [A] Tajogaite 2021, red circles – whole-rock lavas and tephras, see text and Figures 4–6 for the validity of compositionally grouping these two explosive deposits, (data from this study), lines of best fit through the data in all graphs are spline functions with nine cross-median knots calculated using `Stata` statistical software; [B] Kīlauea 2018, whole-rock lavas, white diamonds – 'conventional' X-ray fluorescence spectroscopy data, dark grey diamonds – 'rapid' energy dispersive X-ray spectroscopy data, note the clear and consistent overlap between the two datasets (data from Gansecki et al. [2019]); [C] Fagradalsfjall 2021, light grey diamonds – whole-rock lavas (data from Bindeman et al. [2022]). All data are recalculated to 100 wt.% dry with Fe recalculated as FeOT, expressed as wt.%. Note the systematic ~0.5 wt.% reduction in MgO 15–20 days before the end of each eruptive period.

by reconstructing the eruption-ending magmatic mechanism from the lava, tephra and tephra glass compositions. Not all eruptions are hybrid like Tajogaite, nevertheless our results have identified a signal that may be common to effusive and explosive activity, which would have obvious implications for forecasting the end of future paroxysms elsewhere.

Intriguingly, the geochemical signals apparently identifying eruption shutdown, e.g. Stage 3 reduction in deep mantle-derived MgO-rich magma, is evident in other recent eruptions (Figure 9). Time-resolved datasets from the 2018 Kīlauea, Hawai'i [Gansecki et al. 2019] and 2021 Fagradalsfjall eruptions [Bindeman et al. 2022; Halldórsson et al. 2022] show similar variations to the Tajogaite lavas, for example, an initial sharp increase in MgO followed by some decrease in MgO the weeks leading up to the end of activity (Figure 9). It should be borne in mind, however, that although the volcanism in Hawai'i marks a discreet eruptive cycle, the Iceland data may be considered more a hiatus than the end of activity.

The 2018 eruption of Kīlauea began on 3rd May with opening of the lower East Rift Zone fissure and ended 127 days later on 5th September. Gansecki et al. [2019] defined 4 stages for the eruption. Similarity in the evolution of the early eruptive phases with those of the Tajogaite eruption are clear, of particular note is the shift to eruption of more mafic, hotter, less viscous lavas a week after activity began. Tantalisingly, the last effusion, sampled on day 94 of Phase 3 (due to lava inaccessibility beyond that time), was a lower MgO, more crystal-rich lava interpreted as older and more evolved originating from stored magma system mush (Figure 9B, Gansecki et al. [2019]).

The 2021 eruption of Fagradalsfjall, Iceland, began on March 19 and lasted until mid-September almost 180 days later. It was the first activity in 781 years in what has become a series of eruptions on the Reykjanes Peninsula. Both the start and end of the Fagradalsfjall eruption show compositional trends and timings similar to variations observed in the Tajogaite time series (Figure 9C). The initially lowest values of MgO remained constant for approximately one week before gradually increasing through the first month of the eruption, related to deepening of magma extraction [Bindeman et al. 2022; Halldórsson et al. 2022]. Then, compositions plateaued before a decrease in whole-rock lava MgO became evident some three quarters of the way through the eruptive cycle (Figure 9C).

Given the similarities in three recent mafic eruptive sequences, the value of integrating petrological data into future volcanic response is clear. Considering the utility of datasets that may be obtained syn-eruptively during a volcanic crisis depends on the ease and rapidity of obtaining the data and what results reveal. Without devaluing other techniques, we favour prioritising petrographic description and major and trace element analysis of whole-rock lava and tephra [cf.

Gansecki et al. 2019; Bindeman et al. 2022; Halldórsson et al. 2022]; these show clear changes and yield insights into the evolution of the magmatic system perhaps foreshadowing eruptive shutdown. Essential major elements and ratios to interpret include SiO_2, MgO, FeO, CaO/Al_2O_3, and K_2O/TiO_2; and traces Ni, Cr, Zr, Sc, La/Yb, and Nb/Zr (Figures 5 and 6). In this context it is worth bearing in mind the use of energy dispersive and portable (p)XRF to rapidly and cheaply complement traditional analytical methods.

Timely, relevant data can only be produced if infrastructure and personnel are already in place for sample collection, transportation and analysis prior to, or immediately after, eruption onset. As Re et al. [2021] concluded, onsite facilities and skilled staff greatly enhance the effectiveness of petrological monitoring. A notable limitation of the current study was the time required to organise logistics for sample transport, underscoring the importance of preparedness before an eruption begins. We endorse future developments suggested by Re et al. [2021] to achieve real-time petrological monitoring including: preparedness training; increased cooperation and data exchange between monitoring scientists and volcano observatories; global protocols for systematic sampling and essential analyses; mobile laboratories and automated instrumentation; adoption of emerging technologies such as scanning μXRF, X-ray micro-computed tomography; and streamlining of sample preparation and analytical techniques for important methodologies such as diffusion chronometry.

In addition to advancing understanding of volcanic processes, application of both hindcasting and forecasting are critical for informing decision-making in communities living with volcanoes to improve risk and hazard assessment and management. Past activity strongly suggests volcanism will recur along the Cumbre Vieja ridge and therefore, it is critical to identify causative links between the petrological record of erupted deposits and real-time monitoring signals including seismicity [D'Auria et al. 2022], ground deformation [Charco et al. 2024], and lava discharge rate [Bonadonna et al. 2022].

The relevance of such applications has been highlighted recently in Hawai'i [Gansecki et al. 2019], Sicily [Corsaro and Miraglia 2022], and Iceland [Bindeman et al. 2022; Halldórsson et al. 2022]. Establishing such connections for the Tajogaite eruption will inform future hazard assessment and risk management on La Palma, more broadly in the Canaries and also for similar basaltic systems worldwide.

8 Conclusions and implications

We use petrological characteristics to describe the Tajogaite eruption as having three main stages based on whole-rock compositions: initiation (Stage 1), tapping-evacuating (Stage 2), and waning (Stage 3). During Stage 1, an influx of deep, primitive magma perturbed an evolved, hydrous crystal mush that was rapidly mobilised and erupted as ante- and/or xenocryst-bearing material. Stage 2 progressively evacuated magma with compositional variation resulting from pre-eruptive fractional crystallisation and minor contamination, rather than tapping of distinct mantle sources. Major and trace element values in lavas and tephra trended to more primitive compositions reflecting eruption of magma from shallow to deep storage, and from higher to lower mobility. Finally, Stage 3 was characterised by more evolved glass compositions, but unchanging mineral proportions and compositions, giving the appearance of a fractionated magma. Instead, this stage was driven by the extraction of interstitial melt through filter pressing of crystal-rich mush lenses as the deep-sourced magma supply shut down leading to system collapse and compression. The collapse of the magma system led to closure of the feeder channels resulting in eruption cessation, heralded by a decoupling between whole-rock and tephra glass composition up to two weeks before it occurred.

Integrating petrological data with other monitoring data streams during volcanic crises provides a more comprehensive picture of volcanic activity. Clear temporal variations in petrological data record dynamic changes in the magma plumbing system. Significant synchronicity exists between changes in lava and tephra compositions and real-time monitoring signals such as earthquake depth and frequency, volcanic tremor amplitude, ground deformation, gas geochemistry and lava discharge rates. Thus, petrology provides crucial data that are directly relevant for decision-making authorities and response teams including information about eruption evolution, changes in potential hazards and, importantly, when the eruption may end. Hence, we support petrological monitoring approaches being added to the toolbox of useful near-real-time surveillance observations for comparable future basaltic eruptions. Determination of salient petrological signals such as those described here and from other eruptions and volcanic systems will help formulate the most efficient petrological protocols. Such procedures will determine which data should be prioritised in volcanic monitoring as part of future scientific responses to volcanic crises, in order to protect lives, livelihoods and properties.

Author Contributions

JHS: conceptualisation, formal analysis, investigation, writing - original draft and review and editing, visualisation; MJP: conceptualisation, software, formal analysis, investigation, writing - original draft and review and editing, visualisation; OAB: conceptualisation, formal analysis, investigation, writing - original draft and review and editing, visualisation; KJC: conceptualisation, investigation, data curation, supervision, project administration, funding acquisition, writing - original draft and review and editing, visualisation; DJM: conceptualisation; DAN: investigation, writing - review and editing; JH: investigation, writing - review and editing; MAL: validation, formal analysis, investigation, visualisation, supervision, project administration, funding acquisition; ST: validation, formal analysis, investigation, visualisation; PW: investigation, writing - review and editing; BCC: investigation; WH: visualisation; AGS: software, investigation, writing supplementary material; GKR: analysis, investigation, data curation; LD: visualisation; NMP: funding acquisition.

Acknowledgements

A large number of colleagues are thanked for field assistance and are named in Supplementary Material 1 whole-rock data, tab 2 'samples'. We are grateful to John Browning for his positive and constructive editorial handling, to Jamie Farquharson for his meticulous typesetting, and to two anonymous reviewers for the time and effort they took to help us improve the clarity and rigour of our data presentation and interpretations. Funding sources: VOLRISKMAC (MAC/3.5b/124), VOLRISKMAC II (MAC2/3.5b/328); European Commission Program INTERREG V A Spain-Portugal MAC 2014-2020; Cumbre Vieja Emergencia, Science and Innovation Ministry, Spanish Government; TFassistance, Cabildo Insular de Tenerife; LPvolcano, Cabildo Insular de La Palma; and NERC urgency grant NE/W007673/1.

Data Availability

Full datasets are available as supplementary information: Supplementary Material 1—whole-rock data; Supplementary Material 2—mantle modelling and QEMSCAN® images; Supplementary Material 3—fractional crystallisation modelling.

Copyright notice

References

Amonte, C., G. V. Melián, M. Asensio-Ramos, N. M. Pérez, E. Padrón, P. A. Hernández, and L. D'Auria (2022). "Hydrogeochemical temporal variations related to the recent volcanic eruption at the Cumbre Vieja Volcano, La Palma, Canary Islands". *Frontiers in Earth Science* 10. DOI: 10.3389/feart.2022.1003890.

Anderson Jr, A. T., G. H. Swihart, G. Artioli, and C. A. Geiger (1984). "Segregation vesicles, gas filter-pressing, and igneous differentiation". *The Journal of Geology* 92(1), pages 55–72.

Barclay, J., R. Few, M. T. Armijos, J. C. Phillips, D. M. Pyle, A. Hicks, S. K. Brown, and R. E. A. Robertson (2019). "Livelihoods, Wellbeing and the Risk to Life During Volcanic Eruptions". *Frontiers in Earth Science* 7. DOI: 10.3389/feart.2019.00205.

Barker, A. K., V. R. Troll, J. C. Carracedo, and P. A. Nicholls (2015). "The magma plumbing system for the 1971 Teneguía eruption on La Palma, Canary Islands". *Contributions to Mineralogy and Petrology* 170(5–6). DOI: 10.1007/s00410-015-1207-7.

Bindeman, I. N., F. M. Deegan, V. R. Troll, T. Thordarson, Á. Höskuldsson, W. M. Moreland, E. U. Zorn, A. V. Shevchenko, and T. R. Walter (2022). "Diverse mantle components with invariant oxygen isotopes in the 2021 Fagradalsfjall eruption, Iceland". *Nature Communications* 13(1). DOI: 10.1038/s41467-022-31348-7.

Blundy, J. and K. Cashman (2008). "Petrologic Reconstruction of Magmatic System Variables and Processes". *Mineral inclusions and volcanic processes (Reviews in Mineralogy and Geochemistry)*. Edited by K. D. Putirka and F. J. T. III. Volume 69. 1. Mineralogical Society of America, pages 179–239. DOI: 10.2138/rmg.2008.69.6.

Bohrson, W. A., F. J. Spera, J. S. Heinonen, G. A. Brown, M. A. Scruggs, J. V. Adams, M. K. Takach, G. Zeff, and E. Suikkanen (2020). "Diagnosing open-system magmatic processes using the Magma Chamber Simulator (MCS): part I—major elements and phase equilibria". *Contributions to Mineralogy and Petrology* 175(11). DOI: 10.1007/s00410-020-01722-z.

Bonadonna, C., M. Pistolesi, S. Biass, M. Voloschina, J. Romero, D. Coppola, A. Folch, L. D'Auria, A. Martin-Lorenzo, L. Dominguez, C. Pastore, M.-P. Reyes Hardy, and F. Rodríguez (2022). "Physical Characterization of Long-Lasting Hybrid Eruptions: The 2021 Tajogaite Eruption of Cumbre Vieja (La Palma, Canary Islands)". *Journal of Geophysical Research: Solid Earth* 127(11). DOI: 10.1029/2022jb025302.

Bonechi, B., M. Polacci, F. Arzilli, J. Romero, J. Fellowes, and M. Burton (2024). "Magma residence time, ascent rate and eruptive style of the November ash-laden activity during the 2021 Tajogaite eruption (La Palma, Spain)". *Volcanica* 7(1), pages 51–65. DOI: 10.30909/vol.07.01.5165.

Bowen, N. L. (1928). *Evolution of the Igneous Rocks*. Princeton: Princeton University Press. 334 pages.

Burton, M., A. Aiuppa, P. Allard, M. Asensio-Ramos, A. P. Cofrades, A. La Spina, E. J. Nicholson, V. Zanon, J. Barrancos, M. Bitetto, M. Hartley, J. E. Romero, E. Waters, A. Stewart, P. A. Hernández, J. P. Lages, E. Padrón, K. Wood, B. Esse, C. Hayer, K. Cyrzan, E. F. Rose-Koga, F. Schiavi, L. D'Auria, and N. M. Pérez (2023). "Exceptional eruptive CO2 emissions from intra-plate alkaline magmatism in the Canary volcanic archipelago". *Communications Earth & Environment* 4(1). DOI: 10.1038/s43247-023-01103-x.

Cabrera Pérez, I., L. D'Auria, J. Soubestre, M. Przeor, I. Koulakov, D. Martínez van Dorth, J. M. Ibáñez, V. Ortega, J. Barrancos, G. D. Padilla, R. García-Hernández, and N. Pérez (2022). "Spatio-temporal velocity variations observed during the pre-eruptive episode of La Palma eruption inferred from ambient noise interferometry". DOI: 10.5194/egusphere-egu22-5133.

Caracciolo, A., M. Kahl, E. Bali, G. H. Guðfinnsson, S. A. Halldórsson, and M. E. Hartley (2021). "Timescales of crystal mush mobilization in the Bárðarbunga-Veiðivötn volcanic system based on olivine diffusion chronometry". *American Mineralogist* 106(7), pages 1083–1096. DOI: 10.2138/am-2021-7670.

Carracedo, J. C., E. R. Badiola, H. Guillou, J. De la Nuez, and F. J. Pérez Torrado (2001). "Geología y vulcanología de La Palma y El Hierro, Canarias Occidentales". *Estudios Geológicos* 57(5–6). DOI: 10.3989/egeol.01575-6134.

Carracedo, J. C. and V. R. Troll (2016). *The geology of the Canary Islands*. Amsterdam: Elsevier. 621 pages. ISBN: 978-0-12-809663-5.

Cashman, K. V., R. S. J. Sparks, and J. D. Blundy (2017). "Vertically extensive and unstable magmatic systems: A unified view of igneous processes". *Science* 355(6331). DOI: 10.1126/science.aag3055.

Cassidy, M., M. Manga, K. Cashman, and O. Bachmann (2018). "Controls on explosive-effusive volcanic eruption styles".

Nature Communications 9(1). DOI: 10.1038/s41467-018-05293-3.
Castro, J. M. and Y. Feisel (2022). "Eruption of ultralow-viscosity basanite magma at Cumbre Vieja, La Palma, Canary Islands". *Nature Communications* 13(1). DOI: 10.1038/s41467-022-30905-4.
Chang, W.-L., R. B. Smith, C. Wicks, J. M. Farrell, and C. M. Puskas (2007). "Accelerated Uplift and Magmatic Intrusion of the Yellowstone Caldera, 2004 to 2006". *Science* 318(5852), pages 952–956. DOI: 10.1126/science.1146842.
Charco, M., P. J. González, J. L. G. Pallero, L. García-Cañada, C. del Fresno, and A. Rodríguez-Ortega (2024). "The 2021 La Palma (Canary Islands) Eruption Ending Forecast Through Magma Pressure Drop". *Geophysical Research Letters* 51(10). DOI: 10.1029/2023gl106885.
Comisión mixta para la reconstrucción, recuperación y apoyo a la isla de La Palma, integrada por el Gobierno De España, el Gobierno De Canarias, el Cabildo De La Palma y los ayuntamientos de Los Llanos De Aridane, El Paso y Tazacorte (2022). *Informe sobre las actuaciones y medidas emprendidas tras la erupción del volcán de Cumbre Vieja (La Palma), seis meses después del inicio de la emergencia*. Governement Report. Madrid.
Connolly, J. A. D., M. W. Schmidt, G. Solferino, and N. Bagdassarov (2009). "Permeability of asthenospheric mantle and melt extraction rates at mid-ocean ridges". *Nature* 462(7270), pages 209–212. DOI: 10.1038/nature08517.
Corsaro, R. A. and L. Miraglia (2022). "Near Real-Time Petrologic Monitoring on Volcanic Glass to Infer Magmatic Processes During the February–April 2021 Paroxysms of the South-East Crater, Etna". *Frontiers in Earth Science* 10. DOI: 10.3389/feart.2022.828026.
Corsaro, R. A., L. Miraglia, I. Arienzo, and V. Di Renzo (2024). "The 2020–2022 paroxysmal episodes of the South-East Crater (Mt. Etna): insights into high-frequency eruptive activity from petrological monitoring". *Bulletin of Volcanology* 86(10). DOI: 10.1007/s00445-024-01770-4.
Costa, F., L. A. Coogan, and S. Chakraborty (2010). "The time scales of magma mixing and mingling involving primitive melts and melt–mush interaction at mid-ocean ridges". *Contributions to Mineralogy and Petrology* 159(3), pages 371–387. DOI: 10.1007/s00410-009-0432-3.
D'Auria, L., I. Koulakov, J. Prudencio, I. Cabrera-Pérez, J. M. Ibáñez, J. Barrancos, R. García-Hernández, D. Martínez van Dorth, G. D. Padilla, M. Przeor, V. Ortega, P. Hernández, and N. M. Peréz (2022). "Rapid magma ascent beneath La Palma revealed by seismic tomography". *Scientific Reports* 12(1). DOI: 10.1038/s41598-022-21818-9.
Day, J. M. D., J. C. Carracedo, H. Guillou, and P. Gravestock (1999). "Recent structural evolution of the Cumbre Vieja volcano, La Palma, Canary Islands: volcanic rift zone reconfiguration as a precursor to volcano flank instability?" *Journal of Volcanology and Geothermal Research* 94(1–4), pages 135–167. DOI: 10.1016/s0377-0273(99)00101-8.
Day, J. M. D., V. R. Troll, M. Aulinas, F. M. Deegan, H. Geiger, J. C. Carracedo, G. G. Pinto, and F. J. Perez-Torrado (2022). "Mantle source characteristics and magmatic processes during the 2021 La Palma eruption". *Earth and Planetary Science Letters* 597, page 117793. DOI: 10.1016/j.epsl.2022.117793.
Dayton, K., E. Gazel, P. Wieser, V. R. Troll, J. C. Carracedo, M. Aulinas, and F. J. Perez-Torrado (2024). "Magmatic Storage and Volatile Fluxes of the 2021 La Palma Eruption". *Geochemistry, Geophysics, Geosystems* 25(6). DOI: 10.1029/2024gc011491.
Dayton, K., E. Gazel, P. Wieser, V. R. Troll, J. C. Carracedo, H. La Madrid, D. C. Roman, J. Ward, M. Aulinas, H. Geiger, F. M. Deegan, G. Gisbert, and F. J. Perez-Torrado (2023). "Deep magma storage during the 2021 La Palma eruption". *Science Advances* 9(6). DOI: 10.1126/sciadv.ade7641.
Del Fresno, C., S. Cesca, A. Klügel, I. Domínguez Cerdeña, E. A. Díaz-Suárez, T. Dahm, L. García-Cañada, S. Meletlidis, C. Milkereit, C. Valenzuela-Malebrán, R. López-Díaz, and C. López (2023). "Magmatic plumbing and dynamic evolution of the 2021 La Palma eruption". *Nature Communications* 14(1). DOI: 10.1038/s41467-023-35953-y.
Devine, J. D., M. J. Rutherford, and J. E. Gardner (1998). "Petrologic determination of ascent rates for the 1995–1997 Soufriere Hills Volcano andesitic magma". *Geophysical Research Letters* 25(19), pages 3673–3676. DOI: 10.1029/98gl00912.
Di Paolo, F., J. Ledo, K. Ślęzak, D. Martínez van Dorth, I. Cabrera-Pérez, and N. M. Pérez (2020). "La Palma island (Spain) geothermal system revealed by 3D magnetotelluric data inversion". *Scientific Reports* 10(1). DOI: 10.1038/s41598-020-75001-z.
Dosseto, A., S. P. Turner, and J. A. Van-Orman (2010). *Timescales of magmatic processes: from core to atmosphere*. John Wiley & Sons. ISBN: 978-1-44-433260-5.
Ebmeier, S. K., B. J. Andrews, M. C. Araya, D. W. D. Arnold, J. Biggs, C. Cooper, E. Cottrell, M. Furtney, J. Hickey, J. Jay, R. Lloyd, A. L. Parker, M. E. Pritchard, E. Robertson, E. Venzke, and J. L. Williamson (2018). "Synthesis of global satellite observations of magmatic and volcanic deformation: implications for volcano monitoring & the lateral extent of magmatic domains". *Journal of Applied Volcanology* 7(1). DOI: 10.1186/s13617-018-0071-3.
Eibl, E. P. S., T. Thordarson, Á. Höskuldsson, E. Á. Gudnason, T. Dietrich, G. P. Hersir, and T. Ágústsdóttir (2023). "Evolving shallow conduit revealed by tremor and vent activity observations during episodic lava fountaining of the 2021 Geldingadalir eruption, Iceland". *Bulletin of Volcanology* 85(2). DOI: 10.1007/s00445-022-01622-z.
Ewart, J. A., B. Voight, and A. Björnsson (1991). "Elastic deformation models of Krafla Volcano, Iceland, for the decade 1975 through 1985". *Bulletin of Volcanology* 53(6), pages 436–459. DOI: 10.1007/bf00258184.
Fabbrizio, A., E. C. Bamber, E. Michailidou, J. E. Romero, F. Arzilli, B. Bonechi, M. Polacci, and M. Burton (2023). "Phase equilibrium experiments and thermodynamic simulations to constrain the pre-eruptive conditions of the 2021 Tajogaite eruption (Cumbre Vieja volcano, La Palma, Canary Islands)". *Journal of Volcanology and Geothermal Research* 442, page 107901. DOI: 10.1016/j.jvolgeores.2023.107901.

Fernández, J., J. Escayo, A. G. Camacho, M. Palano, J. F. Prieto, Z. Hu, S. V. Samsonov, K. F. Tiampo, and E. Ancochea (2022). "Shallow magmatic intrusion evolution below La Palma before and during the 2021 eruption". *Scientific Reports* 12(1). DOI: 10.1038/s41598-022-23998-w.

Frontoni, A., A. Costa, A. Vona, and C. Romano (2022). "A comprehensive database of crystal-bearing magmas for the calibration of a rheological model". *Scientific Data* 9(1). DOI: 10.1038/s41597-022-01363-w.

Galipp, K., A. Klügel, and T. H. Hansteen (2006). "Changing depths of magma fractionation and stagnation during the evolution of an oceanic island volcano: La Palma (Canary Islands)". *Journal of Volcanology and Geothermal Research* 155(3–4), pages 285–306. DOI: 10.1016/j.jvolgeores.2006.04.002.

Gansecki, C., R. L. Lee, T. Shea, S. P. Lundblad, K. Hon, and C. Parcheta (2019). "The tangled tale of Kīlauea's 2018 eruption as told by geochemical monitoring". *Science* 366(6470). DOI: 10.1126/science.aaz0147.

Global Volcanism Program (GVP) (2022). "Report on La Palma (Spain)". Edited by K. L. Bennis and E. Venzke. Volume 47. 2. Smithsonian Institution. DOI: 10.5479/si.gvp.bgvn202202-383010.

Gottlieb, P., G. Wilkie, D. Sutherland, E. Ho-Tun, S. Suthers, K. Perera, B. Jenkins, S. Spencer, A. Butcher, and J. Rayner (2000). "Using quantitative electron microscopy for process mineralogy applications". *JOM* 52(4), pages 24–25. DOI: 10.1007/s11837-000-0126-9.

Guillou, H., J. C. Carracedo, and S. J. Day (1998). "Dating of the Upper Pleistocene–Holocene volcanic activity of La Palma using the unspiked K–Ar technique". *Journal of Volcanology and Geothermal Research* 86(1–4), pages 137–149. DOI: 10.1016/s0377-0273(98)00074-2.

Guillou, H., J. C. Carracedo, and R. A. Duncan (2001). "K–Ar, 40Ar–39Ar ages and magnetostratigraphy of Brunhes and Matuyama lava sequences from La Palma Island". *Journal of Volcanology and Geothermal Research* 106(3–4), pages 175–194. DOI: 10.1016/s0377-0273(00)00294-8.

Halldórsson, S. A., E. W. Marshall, A. Caracciolo, S. Matthews, E. Bali, M. B. Rasmussen, E. Ranta, J. G. Robin, G. H. Guðfinnsson, O. Sigmarsson, J. Maclennan, M. G. Jackson, M. J. Whitehouse, H. Jeon, Q. H. A. van der Meer, G. K. Mibei, M. H. Kalliokoski, M. M. Repczynska, R. H. Rúnarsdóttir, G. Sigurðsson, M. A. Pfeffer, S. W. Scott, R. Kjartansdóttir, B. I. Kleine, C. Oppenheimer, A. Aiuppa, E. Ilyinskaya, M. Bitetto, G. Giudice, and A. Stefánsson (2022). "Rapid shifting of a deep magmatic source at Fagradalsfjall volcano, Iceland". *Nature* 609(7927), pages 529–534. DOI: 10.1038/s41586-022-04981-x.

Harris, C. R., K. J. Millman, S. J. van der Walt, R. Gommers, P. Virtanen, D. Cournapeau, E. Wieser, J. Taylor, S. Berg, N. J. Smith, R. Kern, M. Picus, S. Hoyer, M. H. van Kerkwijk, M. Brett, A. Haldane, J. F. del Río, M. Wiebe, P. Peterson, P. Gérard-Marchant, K. Sheppard, T. Reddy, W. Weckesser, H. Abbasi, C. Gohlke, and T. E. Oliphant (2020). "Array programming with NumPy". *Nature* 585(7825), pages 357–362. DOI: 10.1038/s41586-020-2649-2.

Hartley, M. E., D. J. Morgan, J. Maclennan, M. Edmonds, and T. Thordarson (2016). "Tracking timescales of short-term precursors to large basaltic fissure eruptions through Fe–Mg diffusion in olivine". *Earth and Planetary Science Letters* 439, pages 58–70. DOI: 10.1016/j.epsl.2016.01.018.

Hernandez-Pacheco, A. and M. C. Valls (1982). "The historic eruptions of La Palma island (Canaries)". *Arquipélago. Série Ciências da Natureza* 3, pages 83–94.

Hildreth, W. (1981). "Gradients in silicic magma chambers: Implications for lithospheric magmatism". *Journal of Geophysical Research: Solid Earth* 86(B11), pages 10153–10192. DOI: 10.1029/jb086ib11p10153.

Hu, H., M. D. Jackson, and J. Blundy (2022). "Melting, Compaction and Reactive Flow: Controls on Melt Fraction and Composition Change in Crustal Mush Reservoirs". *Journal of Petrology* 63(11). DOI: 10.1093/petrology/egac097.

Huppert, H. E. and R. S. J. Sparks (1981). "The fluid dynamics of a basaltic magma chamber replenished by influx of hot, dense ultrabasic magma". *Contributions to Mineralogy and Petrology* 75(3), pages 279–289. DOI: 10.1007/bf01166768.

Kahl, M., S. Chakraborty, F. Costa, M. Pompilio, M. Liuzzo, and M. Viccaro (2013). "Compositionally zoned crystals and real-time degassing data reveal changes in magma transfer dynamics during the 2006 summit eruptive episodes of Mt. Etna". *Bulletin of Volcanology* 75(2). DOI: 10.1007/s00445-013-0692-7.

Kahl, M., E. J. F. Mutch, J. Maclennan, D. J. Morgan, F. Couperthwaite, E. Bali, T. Thordarson, G. H. Guðfinnsson, R. Walshaw, I. Buisman, S. Buhre, Q. H. A. van der Meer, A. Caracciolo, E. W. Marshall, M. B. Rasmussen, C. R. Gallagher, W. M. Moreland, Á. Höskuldsson, and R. A. Askew (2022). "Deep magma mobilization years before the 2021 CE Fagradalsfjall eruption, Iceland". *Geology* 51(2), pages 184–188. DOI: 10.1130/g50340.1.

Katz, R. F., D. W. R. Jones, J. F. Rudge, and T. Keller (2022). "Physics of Melt Extraction from the Mantle: Speed and Style". *Annual Review of Earth and Planetary Sciences* 50(1), pages 507–540. DOI: 10.1146/annurev-earth-032320-083704.

Kent, A. J. R., C. B. Till, and K. M. Cooper (2023). "Start me up: The relationship between volcanic eruption characteristics and eruption initiation mechanisms". *Volcanica* 6(2), pages 161–172. DOI: 10.30909/vol.06.02.161172.

Klügel, A., K. Galipp, K. Hoernle, F. Hauff, and S. Groom (2017). "Geochemical and Volcanological Evolution of La Palma, Canary Islands". *Journal of Petrology* 58(6), pages 1227–1248. DOI: 10.1093/petrology/egx052.

Klügel, A., T. H. Hansteen, and K. Galipp (2005). "Magma storage and underplating beneath Cumbre Vieja volcano, La Palma (Canary Islands)". *Earth and Planetary Science Letters* 236(1–2), pages 211–226. DOI: 10.1016/j.epsl.2005.04.006.

Klügel, A., K. A. Hoernle, H.-U. Schmincke, and J. D. L. White (2000). "The chemically zoned 1949 eruption on La Palma (Canary Islands): Petrologic evolution and magma supply dynamics of a rift zone eruption". *Journal of Geophysical Research: Solid Earth* 105(B3), pages 5997–6016. DOI: 10.1029/1999jb900334.

Klügel, A., M.-A. Longpré, L. García-Cañada, and J. Stix (2015). "Deep intrusions, lateral magma transport and related uplift at ocean island volcanoes". *Earth and Planetary Science Letters* 431, pages 140–149. DOI: 10.1016/j.epsl.2015.09.031.

Komar, P. D. (1972). "Flow Differentiation in Igneous Dikes and Sills: Profiles of Velocity and Phenocryst Concentration". *Geological Society of America Bulletin* 83(11), page 3443. DOI: 10.1130/0016-7606(1972)83[3443:fdiida]2.0.co;2.

Koulakov, I., L. D'Auria, J. Prudencio, I. Cabrera-Pérez, J. Barrancos, G. D. Padilla, S. Abramenkov, N. M. Pérez, and J. M. Ibáñez (2023). "Local Earthquake Seismic Tomography Reveals the Link Between Crustal Structure and Volcanism in Tenerife (Canary Islands)". *Journal of Geophysical Research: Solid Earth* 128(3). DOI: 10.1029/2022jb025798.

Liao, Y. (2022). "The Roles of Heat and Gas in a Mushy Magma Chamber". *Journal of Geophysical Research: Solid Earth* 127(7). DOI: 10.1029/2022jb024357.

Lissenberg, C. J., C. J. MacLeod, and E. N. Bennett (2019). "Consequences of a crystal mush-dominated magma plumbing system: a mid-ocean ridge perspective". *Philosophical Transactions of the Royal Society A: Mathematical, Physical and Engineering Sciences* 377(2139), page 20180014. DOI: 10.1098/rsta.2018.0014.

Longpré, M.-A. and A. Felpeto (2021). "Historical volcanism in the Canary Islands; part 1: A review of precursory and eruptive activity, eruption parameter estimates, and implications for hazard assessment". *Journal of Volcanology and Geothermal Research* 419, page 107363. DOI: 10.1016/j.jvolgeores.2021.107363.

Longpré, M.-A., S. Tramontano, M. J. Pankhurst, D. C. Roman, M. C. Reiss, F. Cortese, M. R. James, L. Spina, F. Rodríguez, B. Coldwell, A. Martín-Lorenzo, O. Barbee, L. D'Auria, K. J. Chamberlain, and J. H. Scarrow (2024). "Shifting melt composition linked to volcanic tremor at Cumbre Vieja volcano". *Nature Geoscience*. DOI: 10.1038/s41561-024-01623-x.

Marsh, B. D. (1981). "On the crystallinity, probability of occurrence, and rheology of lava and magma". *Contributions to Mineralogy and Petrology* 78(1), pages 85–98. DOI: 10.1007/bf00371146.

McDonough, W. and S.-s. Sun (1995). "The composition of the Earth". *Chemical Geology* 120(3–4), pages 223–253. DOI: 10.1016/0009-2541(94)00140-4.

McKenzie, D. (1984). "The Generation and Compaction of Partially Molten Rock". *Journal of Petrology* 25(3), pages 713–765. DOI: 10.1093/petrology/25.3.713.

Meletlidis, S., A. Di Roberto, M. Pompilio, A. Bertagnini, I. Iribarren, A. Felpeto, P. A. Torres, and C. D'Oriano (2012). "Xenopumices from the 2011–2012 submarine eruption of El Hierro (Canary Islands, Spain): Constraints on the plumbing system and magma ascent". *Geophysical Research Letters* 39(17). DOI: 10.1029/2012gl052675.

Mollo, S. and J. E. Hammer (2017). "Dynamic crystallization in magmas". *Mineral reaction kinetics: Microstructures, textures, chemical and isotopic signatures*. Edited by W. Heinrich and R. Abart. Volume 16. European Mineralogical Union, Notes in Mineralogy, pages 373–418. ISBN: 978-0903056-63-2.

Muñoz, V., T. R. Walter, E. U. Zorn, A. V. Shevchenko, P. J. González, D. Reale, and E. Sansosti (2022). "Satellite Radar and Camera Time Series Reveal Transition from Aligned to Distributed Crater Arrangement during the 2021 Eruption of Cumbre Vieja, La Palma (Spain)". *Remote Sensing* 14(23), page 6168. DOI: 10.3390/rs14236168.

Nakagawa, M., K. Wada, and C. P. Wood (2002). "Mixed Magmas, Mush Chambers and Eruption Triggers: Evidence from Zoned Clinopyroxene Phenocrysts in Andesitic Scoria from the 1995 Eruptions of Ruapehu Volcano, New Zealand". *Journal of Petrology* 43(12), pages 2279–2303. DOI: 10.1093/petrology/43.12.2279.

Natland, J. H. and H. J. B. Dick (2001). "Formation of the lower ocean crust and the crystallization of gabbroic cumulates at a very slowly spreading ridge". *Journal of Volcanology and Geothermal Research* 110(3–4), pages 191–233. DOI: 10.1016/s0377-0273(01)00211-6.

Neave, D. A., I. Buisman, and J. Maclennan (2017). "Continuous mush disaggregation during the long-lasting Laki fissure eruption, Iceland". *American Mineralogist* 102(10), pages 2007–2021. DOI: 10.2138/am-2017-6015ccby.

Neave, D. A. and K. D. Putirka (2017). "A new clinopyroxene-liquid barometer, and implications for magma storage pressures under Icelandic rift zones". *American Mineralogist* 102(4), pages 777–794. DOI: 10.2138/am-2017-5968.

Padrón, E., N. M. Pérez, P. A. Hernández, H. Sumino, G. V. Melián, M. Alonso, F. Rodríguez, M. Asensio-Ramos, and L. D'Auria (2022). "Early Precursory Changes in the 3He/4He Ratio Prior to the 2021 Tajogaite Eruption at Cumbre Vieja Volcano, La Palma, Canary Islands". *Geophysical Research Letters* 49(18). DOI: 10.1029/2022gl099992.

Pankhurst, M. J., K. J. Dobson, D. J. Morgan, S. C. Loughlin, T. Thordarson, P. D. Lee, and L. Courtois (2014). "Monitoring the Magmas Fuelling Volcanic Eruptions in Near-real-time Using X-ray Micro-computed Tomography". *Journal of Petrology* 55(3), pages 671–684. DOI: 10.1093/petrology/egt079.

Pankhurst, M. J., D. J. Morgan, T. Thordarson, and S. C. Loughlin (2018). "Magmatic crystal records in time, space, and process, causatively linked with volcanic unrest". *Earth and Planetary Science Letters* 493, pages 231–241. DOI: 10.1016/j.epsl.2018.04.025.

Pankhurst, M. J., J. H. Scarrow, O. A. Barbee, J. Hickey, B. C. Coldwell, G. K. Rollinson, J. A. Rodríguez-Losada, A. Martín Lorenzo, F. Rodríguez, W. Hernández, D. Calvo Fernández, P. A. Hernández, and N. M. Pérez (2022). "Rapid response petrology for the opening eruptive phase of the 2021 Cumbre Vieja eruption, La Palma, Canary Islands". *Volcanica* 5(1), pages 1–10. DOI: 10.30909/vol.05.01.0110.

Papale, P., C. P. Montagna, and A. Longo (2017). "Pressure evolution in shallow magma chambers upon buoyancy-driven replenishment". *Geochemistry, Geophysics, Geosystems* 18(3), pages 1214–1224. DOI: 10.1002/2016gc006731.

Passmore, E., J. Maclennan, G. Fitton, and T. Thordarson (2012). "Mush Disaggregation in Basaltic Magma Chambers: Evidence from the ad 1783 Laki Eruption". *Jour-*

nal of Petrology 53(12), pages 2593–2623. DOI: 10.1093/petrology/egs061.

Petford, N., M. A. Koenders, and J. D. Clemens (2020). "Igneous differentiation by deformation". *Contributions to Mineralogy and Petrology* 175(5). DOI: 10.1007/s00410-020-1674-3.

Pirrie, D. and G. K. Rollinson (2011). "Unlocking the applications of automated mineral analysis". *Geology Today* 27(6), pages 226–235. DOI: 10.1111/j.1365-2451.2011.00818.x.

Pistone, M., F. Arzilli, K. J. Dobson, B. Cordonnier, E. Reusser, P. Ulmer, F. Marone, A. G. Whittington, L. Mancini, J. L. Fife, and J. D. Blundy (2015). "Gas-driven filter pressing in magmas: Insights into in-situ melt segregation from crystal mushes". *Geology* 43(8), pages 699–702. DOI: 10.1130/g36766.1.

Portner, R., B. M. Dreyer, D. A. Clague, N. R. Daczko, and P. R. Castillo (2022). "Oceanic Zircon Records Extreme Fractional Crystallization of MORB to Rhyolite on the Alarcon Rise Mid-Ocean Ridge". *Journal of Petrology* 63(6). DOI: 10.1093/petrology/egac040.

Przeor, M., R. Castaldo, L. D'Auria, A. Pepe, S. Pepe, T. Sagiya, G. Solaro, P. Tizzani, J. Barrancos Martínez, and N. Pérez (2024). "Geodetic imaging of magma ascent through a bent and twisted dike during the Tajogaite eruption of 2021 (La Palma, Canary Islands)". *Scientific Reports* 14(1). DOI: 10.1038/s41598-023-50982-9.

Putirka, K. D. (2008). "Thermometers and Barometers for Volcanic Systems". *Reviews in Mineralogy and Geochemistry* 69(1), pages 61–120. DOI: 10.2138/rmg.2008.69.3.

Putirka, K. D., H. Mikaelian, F. Ryerson, and H. Shaw (2003). "New clinopyroxene-liquid thermobarometers for mafic, evolved, and volatile-bearing lava compositions, with applications to lavas from Tibet and the Snake River Plain, Idaho". *American Mineralogist* 88(10), pages 1542–1554. DOI: 10.2138/am-2003-1017.

Ranero, C. R., M. Torne, and E. Banda (1995). "Gravity and multichannel seismic reflection constraints on the lithospheric structure of the Canary Swell". *Marine Geophysical Researches* 17(6), pages 519–534. DOI: 10.1007/bf01204342.

Re, G., R. A. Corsaro, C. D'Oriano, and M. Pompilio (2021). "Petrological monitoring of active volcanoes: A review of existing procedures to achieve best practices and operative protocols during eruptions". *Journal of Volcanology and Geothermal Research* 419, page 107365. DOI: 10.1016/j.jvolgeores.2021.107365.

Rollinson, G. K., J. C. Andersen, R. J. Stickland, M. Boni, and R. Fairhurst (2011). "Characterisation of non-sulphide zinc deposits using QEMSCAN®". *Minerals Engineering* 24(8), pages 778–787. DOI: 10.1016/j.mineng.2011.02.004.

Romero, J. E., M. Burton, F. Cáceres, J. Taddeucci, R. Civico, T. Ricci, M. J. Pankhurst, P. A. Hernández, C. Bonadonna, E. W. Llewellin, M. Pistolesi, M. Polacci, C. Solana, L. D'Auria, F. Arzilli, D. Andronico, F. Rodríguez, M. Asensio-Ramos, A. Martín-Lorenzo, C. Hayer, P. Scarlato, and N. M. Perez (2022). "The initial phase of the 2021 Cumbre Vieja ridge eruption (Canary Islands): Products and dynamics controlling edifice growth and collapse". *Journal of Volcanology and Geothermal Research* 431, page 107642. DOI: 10.1016/j.jvolgeores.2022.107642.

Romero, J. E., E. Morgado, A. Pisello, F. Boschetty, M. Petrelli, F. Cáceres, M. A. Alam, M. Polacci, J. L. Palma, F. Arzilli, F. Vera, R. Gutiérrez, and D. Morgavi (2023). "Pre-eruptive Conditions of the 3 March 2015 Lava Fountain of Villarrica Volcano (Southern Andes)". *Bulletin of Volcanology* 85(1). DOI: 10.1007/s00445-022-01621-0.

Sandoval-Velasquez, A., A. Rizzo, F. Casetta, T. Ntaflos, A. Aiuppa, M. Alonso, E. Padrón, M. Pankhurst, A. Mundl-Petermeier, V. Zanon, and N. Pérez (2023). "The noble gas signature of the 2021 Tajogaite eruption (La Palma, Canary Islands)". *Journal of Volcanology and Geothermal Research* 443, page 107928. DOI: 10.1016/j.jvolgeores.2023.107928.

Schmidt, M. W., M. Forien, G. Solferino, and N. Bagdassarov (2012). "Settling and compaction of olivine in basaltic magmas: an experimental study on the time scales of cumulate formation". *Contributions to Mineralogy and Petrology* 164(6), pages 959–976. DOI: 10.1007/s00410-012-0782-0.

Sisson, T. W. and C. R. Bacon (1999). "Gas-driven filter pressing in magmas". *Geology* 27(7), page 613. DOI: 10.1130/0091-7613(1999)027<0613:gdfpim>2.3.co;2.

Soldati, A., C. Cimarelli, U. Kueppers, F. Cáceres, D. Müller, M. Pankhurst, J. H. Scarrow, N. Perez, and D. B. Dingwell (2024). "Melt viscosity tracks the volcanic and magmatic evolution of the 2021 Tajogaite eruption, La Palma (Canary Islands)". *Journal of Volcanology and Geothermal Research* 455, page 108210. DOI: 10.1016/j.jvolgeores.2024.108210.

Solomatov, V. (2007). "Magma Oceans and Primordial Mantle Differentiation". *Treatise on Geophysics*. Edited by G. Schubert. Elsevier, pages 91–119. ISBN: 9780444527486. DOI: 10.1016/b978-044452748-6.00141-3.

Sparks, R. S. J. and K. V. Cashman (2017). "Dynamic Magma Systems: Implications for Forecasting Volcanic Activity". *Elements* 13(1), pages 35–40. DOI: 10.2113/gselements.13.1.35.

Tenzer, R., M. Bagherbandi, and P. Vajda (2013). "Global model of the upper mantle lateral density structure based on combining seismic and isostatic models". *Geosciences Journal* 17(1), pages 65–73. DOI: 10.1007/s12303-013-0009-z.

Ubide, T., Á. Márquez, E. Ancochea, M. J. Huertas, R. Herrera, J. J. Coello-Bravo, D. Sanz-Mangas, J. Mulder, A. MacDonald, and I. Galindo (2023). "Discrete magma injections drive the 2021 La Palma eruption". *Science Advances* 9(27). DOI: 10.1126/sciadv.adg4813.

Ubide, T., D. A. Neave, M. Petrelli, and M.-A. Longpré (2021). "Editorial: Crystal Archives of Magmatic Processes". *Frontiers in Earth Science* 9. DOI: 10.3389/feart.2021.749100.

United Nations Office for Disaster Risk Reduction (UNDRR) (2022). *Global Assessment Report on Disaster Risk Reduction 2022. Our World at Risk: Transforming Governance for a Resilient Future*. Governement Report. Geneva.

Van der Walt, S., J. L. Schönberger, J. Nunez-Iglesias, F. Boulogne, J. D. Warner, N. Yager, E. Gouillart, and T. Yu

(2014). "scikit-image: image processing in Python". *PeerJ* 2, e453. DOI: 10.7717/peerj.453.

Vergara-Pinto, F., N. O'Grady, A. Fredriksen, J. E. Romero, C. Marchant, R. Walshe, A. Donovan, J. Morin, and M. Szlam (2024). "How residents and volcanoes co-produce risk knowledge: Ways of knowing and affective attunement to the rhythms of Lonquimay volcano, Chile". *Journal of Volcanology and Geothermal Research* 454, page 108180. DOI: 10.1016/j.jvolgeores.2024.108180.

Viccaro, M., M. Giuffrida, E. Nicotra, and R. Cristofolini (2016). "Timescales of magma storage and migration recorded by olivine crystals in basalts of the March–April 2010 eruption at Eyjafjallajökull volcano, Iceland". *American Mineralogist* 101(1), pages 222–230. DOI: 10.2138/am-2016-5365.

Wadge, G., G. S. Mattioli, and R. A. Herd (2006). "Ground deformation at Soufrière Hills Volcano, Montserrat during 1998–2000 measured by radar interferometry and GPS". *Journal of Volcanology and Geothermal Research* 152(1–2), pages 157–173. DOI: 10.1016/j.jvolgeores.2005.11.007.

White, W. M. and E. M. Klein (2014). "Composition of the Oceanic Crust". *Treatise on Geochemistry*. Edited by R. L. Rudnick. Elsevier, pages 457–496. ISBN: 9780080983004. DOI: 10.1016/b978-0-08-095975-7.00315-6.

Wieser, P. E., M. L. M. Gleeson, S. Matthews, C. DeVitre, and E. Gazel (2025). "Determining the pressure-temperature-composition (P-T-X) conditions of magma storage". *Treatise on Geochemistry*. Edited by A. Anbar and D. Weis. 3rd edition. Elsevier, pages 83–151. ISBN: 978-0-323-99763-8. DOI: 10.1016/b978-0-323-99762-1.00024-3.

Wong, Y.-Q. and T. Keller (2023). "A unified numerical model for two-phase porous, mush and suspension flow dynamics in magmatic systems". *Geophysical Journal International* 233(2), pages 769–795. DOI: 10.1093/gji/ggac481.

Xing, C.-M. and C. Y. Wang (2020). "Periodic Mixing of Magmas Recorded by Oscillatory Zoning of the Clinopyroxene Macrocrysts from an Ultrapotassic Lamprophyre Dyke". *Journal of Petrology* 61(11–12). DOI: 10.1093/petrology/egaa103.

Zanon, V., L. D'Auria, F. Schiavi, K. Cyrzan, and M. J. Pankhurst (2024). "Toward a near real-time magma ascent monitoring by combined fluid inclusion barometry and ongoing seismicity". *Science Advances* 10(6). DOI: 10.1126/sciadv.adi4300.

Zellmer, G. F. and C. Annen (2008). "An introduction to magma dynamics". *Geological Society, London, Special Publications* 304(1), pages 1–13. DOI: 10.1144/sp304.1.

Zhou, J.-S., Q. Wang, C.-M. Xing, L. Ma, L.-L. Hao, Q.-W. Li, Z.-L. Wang, and T.-Y. Huang (2021). "Crystal growth of clinopyroxene in mafic alkaline magmas". *Earth and Planetary Science Letters* 568, page 117005. DOI: 10.1016/j.epsl.2021.117005.